Soil Dynamics and Earthquake Engineering 177 (2024) 108403

Contents lists available at ScienceDirect

Soil Dynamics and Earthquake Engineering

journal homepage: www.elsevier.com/locate/soildyn

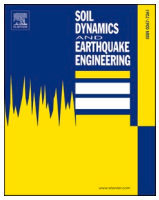

Soil-structure interaction effects on out-of-plane seismic response and damage of masonry buildings with shallow foundations

Francesco Silvestri [a,*], Filomena de Silva [a], Annachiara Piro [a], Fulvio Parisi [b]

[a] Department of Civil, Architectural and Environmental Engineering, University of Naples Federico II, Naples, Italy
[b] Department of Structures for Engineering and Architecture, University of Naples Federico II, Naples, Italy

ARTICLE INFO

Keywords:
Soil-foundation-structure interaction
Masonry building
Replacement oscillator
Fragility function

ABSTRACT

A significant amount of damage and casualties induced by several strong-motion earthquakes which recently stroke South-East Mediterranean area is due to the major seismic vulnerability of residential buildings. In small villages and mid-size towns, those buildings very often consist of two- to four-story, unreinforced masonry (URM) structures not designed for earthquake resistance, with direct foundations usually corresponding to an in-depth extension of load-bearing walls. For such structures, especially when founded on soft soils, site amplification and soil-foundation-structure interaction (SFSI) can significantly affect the seismic performance; conversely, such phenomena should be investigated through methods that allow a trade-off between accuracy and computational effort, hence encouraging their implementation in engineering practice. This paper provides a comprehensive updated description of the studies carried out in the last years by the authors, which are based on both linear and nonlinear, parametric, dynamic analyses of complete soil-foundation-structure (SFS) models representative of existing residential building configurations on different soils. Specifically, the parametric study investigated SFS models with different masonry types, aspect ratios, and code-conforming homogeneous and heterogeneous soil profiles. The methodology and analysis results allowed for reaching the following objectives: (i) predicting the elongation of the fundamental period and the variation of equivalent damping of the SFS system with respect to fixed-base conditions, through a simplified approach based on an equivalent simple oscillator; and (ii) estimating the probability of exceeding increasing damage levels associated with out-of-plane overturning of URM walls, through fragility functions that take into account SFS interaction. The effectiveness of these simplified tools was successfully validated against well-documented case studies, at the scales of both single instrumented buildings and urban area.

1. Introduction

It is well-known that earthquakes are among the natural disasters that most significantly affect the development of many countries, as reported by World Bank [1]. For such a reason, seismic safety of the built heritage is a key priority to limit damages and, consequently, human and economic losses.

Fig. 1 highlights that seismic risk in Europe is maximum in the South-East Mediterranean countries, due to both the significant seismic hazard shown by the European Seismic Hazard Map [2] (Fig. 1a), and the high structural vulnerability [3], as remarked after the recent strong earthquakes that struck Italy [4–6], Greece [7,8] and Croatia [9]. In these countries, the built heritage is particularly vulnerable, because mostly consisting of unreinforced masonry (URM) (see percentages in Fig. 1a) [3,10] and built before the emanation of seismic codes. For such buildings, the lack of structural elements to withstand horizontal actions makes the load-bearing walls subjected to significant out-of-plane (OOP) lateral actions, often resulting in local collapse mechanisms, as shown by the representative pictures shown in Fig. 1b.

In addition, especially in the urban centers located on coastal and alluvial geological formations, URM structures often lay on shallow loose cohesionless or soft cohesive soil deposits which amplify seismic motion [11].

As pointed out by Mylonakis and Gazetas [12], soil-foundation-structure interaction (SFSI) can induce either beneficial or detrimental effects on the seismic performance of structures. As a

* Corresponding author.
E-mail addresses: francesco.silvestri@unina.it (F. Silvestri), filomena.desilva@unina.it (F. de Silva), annachiara.piro@unina.it (A. Piro), fulvio.parisi@unina.it (F. Parisi).

https://doi.org/10.1016/j.soildyn.2023.108403
Received 3 March 2023; Received in revised form 5 October 2023; Accepted 6 December 2023
Available online 27 December 2023

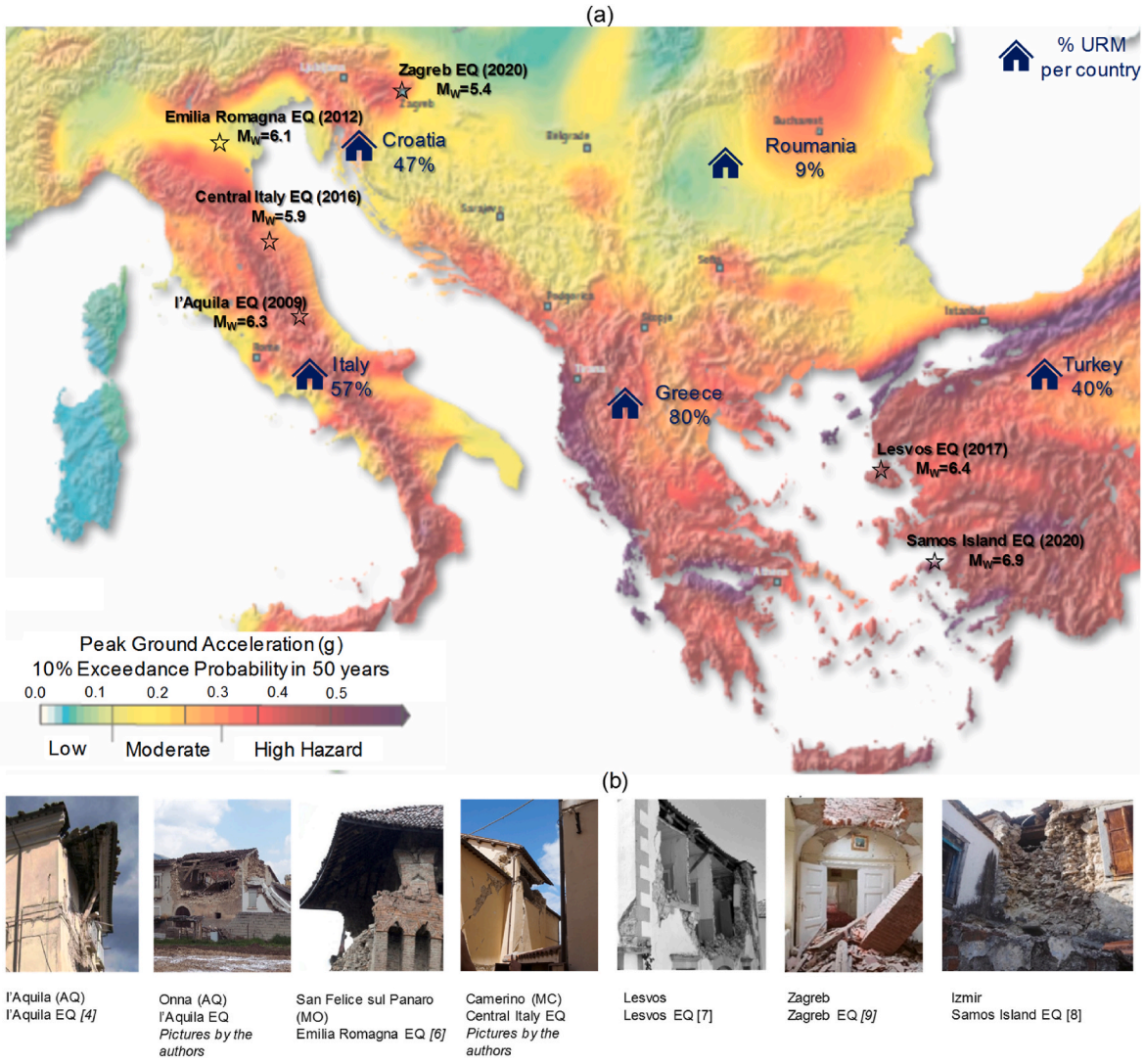

Fig. 1. (a) SHARE seismic hazard map of peak ground acceleration with a probability of exceedance equal to 10% in 50 years [2] and percentage of URM buildings in some European countries [3], (b) masonry buildings damaged by out-of-plane mechanisms in recent seismic events.

matter of fact, parametric analyses by Khosravikia et al. [13] highlighted the role of SFSI on seismic losses by investigating the response of stiff and flexible steel and concrete structures lying on soil profiles with variable deformability. The results showed that SFSI is beneficial in the case of structures on very deformable soils, regardless of their slenderness ratio and foundation embedment, mitigating losses with effectiveness that increases with the structural height. Conversely, in the case of less deformable soils, SFSI can lead to detrimental effects, increasing seismic losses. Notwithstanding this evidence, the seismic vulnerability of buildings is usually assessed under the fixed-based (FB) assumption rather than analyzing the soil-foundation-structure (SFS) system as a whole.

So far, several research studies on SFSI have produced fragility curves for a wide range of soils and building models on reinforced concrete (*e.g.* [14,15]) or steel structures ([16,17]), while very few are those dealing with URM buildings [18,19]. This knowledge gap is mostly due to the high computational demand and modeling effort, which are affordable in case of specific studies on high-value buildings (e.g. [18]) but can result prohibitive in the case of ordinary residential structures. For this reason, Petridis and Pitilakis [20] proposed a method to modify the existing fragility curves for fixed-base structures to consider SFSI effects in large-scale risk assessment. The so-called 'fragility modifiers' were obtained as ratios between the median values of the curves referred to SFS system and FB system, to be multiplied by the median value of the FB fragility curve for each damage level (DL).

All the above-mentioned studies refer to the global response of structures. Very few investigations were carried out on the effects of SFSI on the OOP failure mechanism. In this study, the overturning failure of URM walls associated with their OOP bending and rocking motion is investigated by means of two-dimensional numerical models. This failure mode of URM walls is one of the OOP mechanisms that are typically observed on existing URM buildings after strong earthquakes, as explained in several studies (see, e.g., D'Ayala and Speranza [21]). Other failure modes, such as those involving building corners or spandrels subjected to horizontal bending, are not considered in this study because they ask for different models. For example, Fathi et al. [22] performed modal and nonlinear time history analyses on a coupled 3D model of an ancient building in Iran. The results revealed that SFSI leads to a reduction in terms of acceleration response along the out-of-plane direction, but increases the displacement demand with respect to the fixed-base condition and consequently leads to OOP failure mechanisms.

All the above considerations motivate the need to assess the effects of SFSI on seismic performance and damage of URM buildings, particularly to OOP failure mechanisms that frequently occur in structures of historical urban centers. Thus, the aim of this work was three-fold:

(i) to exploit the results of parametric studies carried out through advanced numerical analyses (Section 4), in order to update the existing formulas for the prediction of period and damping ratio of SFS systems and to make them applicable to typical URM residential buildings;
(ii) to assess SFSI effects on the fragility curves relevant to OOP failure mechanisms of URM buildings, accounting for the variability in geotechnical and structural properties, such as soil deformability, masonry type and building slenderness (Section 5);
(iii) to validate the approach proposed for the estimation of period and damping ratio as well as the obtained fragility curves against well-documented case studies showing, respectively, the influence of SFSI on the dynamic response (Section 4.3) and earthquake-induced damage at territorial scale (Section 5.4).

2. An overview of approaches for SFSI analysis

To account for SFSI effects in seismic performance assessment, soil-structure models have been proposed in the literature with a variable degree of refinement, as depicted in Fig. 2. According to an increasing complexity level, the following alternative structural models can be adopted:

- a single-degree-of-freedom (SDOF) oscillator, defined by a mass, m, a flexural stiffness, k, and a damping ratio, ξ, which is characterized by a single vibration mode and, consequently, by a single natural period (Fig. 2a and d);
- a multi-degree-of-freedom (MDOF) system, defined by a set of n lumped masses, m_i, a stiffness matrix, **K**, and a damping matrix, **C**, which is characterized by n vibration modes (Fig. 2b and e);
- a continuum model, in which each structural element is defined by a mass density, ρ, a shear modulus, G, a Poisson's ratio, ν, and a given shape and size, which is characterized by an infinite number of vibration modes and can be discretized by a numerical technique, such as finite element or finite difference methods (Fig. 2c and f).

On the other hand, soil models with increasing complexity can be identified as follows:

- a set of springs and dashpots characterized by stiffness, K_{ij}, and damping parameters, C_{ij}, related to the translational and rotational components of the foundation motion (Fig. 2a-b-c);
- a continuum model with mass density, ρ, shear modulus, G, Poisson's ratio, ν, characterized by suitable in-depth and lateral extensions as well as by either reflecting or absorbing boundaries (Fig. 2d-e-f).

Needless to say, the structure and soil properties can vary in the continuum models, depending on their degree of heterogeneity, as well as be more complex than the basic elastic or visco-elastic parameters, due to nonlinear material behaviour. In the simplest soil models, the spring stiffness and the viscous dashpot parameters simulating the soil compliance to the foundation motion are calibrated through the impedance functions [23]. They are the sum of a real part representing the dynamic stiffness and an imaginary part accounting for the damping:

$$\overline{K}_{ij} = k_{ij}(a_0)K_{ij} + \mathrm{i}\,\omega c_{ij}\,(a_0)C_{ij} \tag{1}$$

In Eq. (1):

- i is the imaginary unit;

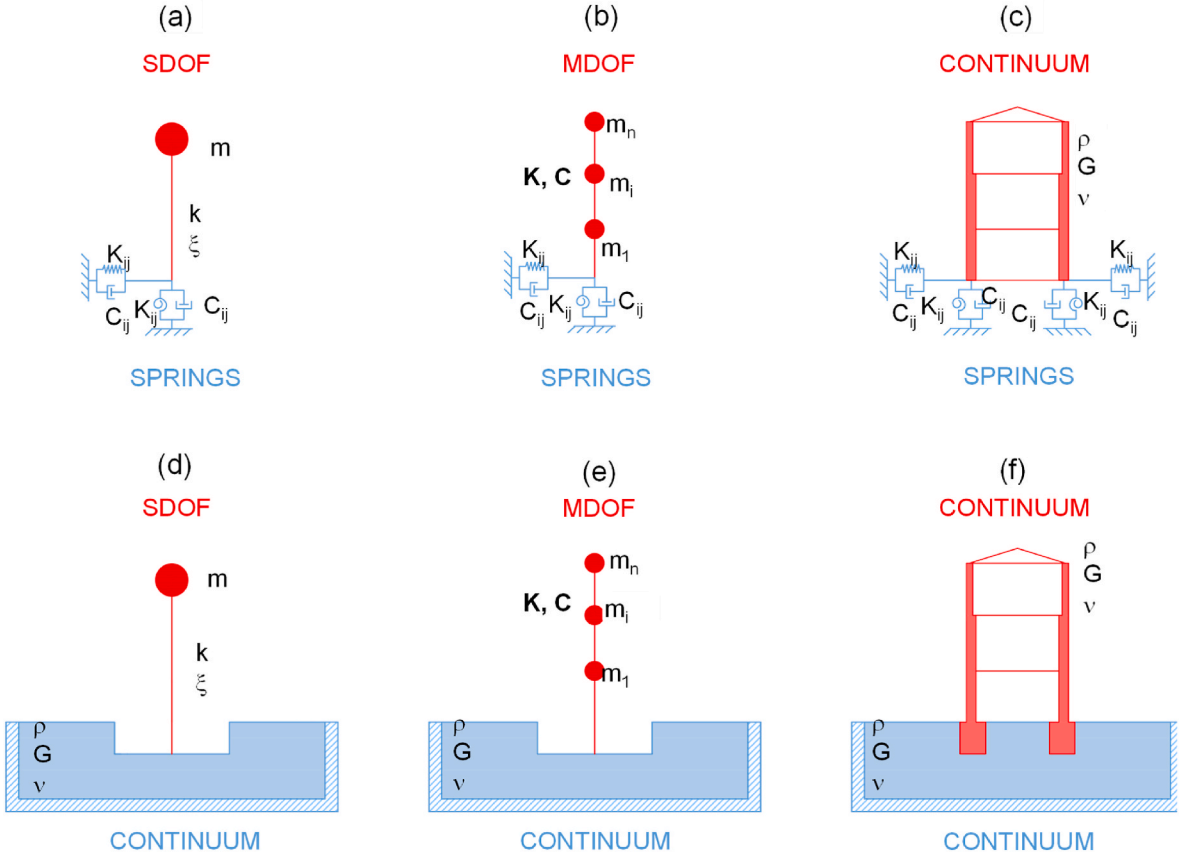

Fig. 2. SFS models with different complexity levels related to the structure and soil: SDOF oscillator, MDOF system, continuum structural model on springs and dashpots (a, b, c), and on continuum soil model (d, e, f). Red and blue colors of the drawings and the labels refer to the structure and soil models, respectively.

- the subscripts *i, j* indicate that $\overline{K}_{ij}$ links the component *i* of the vector of the loads transmitted by the foundation into the soil to the component *j* of the displacement vector;
- the static stiffness, K_{ij}, and the dashpot coefficient, C_{ij}, depend on the soil shear modulus, G, and Poisson's ratio, ν, as well as on a characteristic dimension of the foundation, r;
- the dynamic coefficients, $k_{ij}(a_0)$ and $c_{ij}(a_0)$, are expressed as functions of the vibration frequency, ω, the foundation dimension, r, and the soil shear wave velocity, V_S, through the dimensionless frequency factor, $a_0 = \omega r/V_S$.

The impedance parameters can be experimentally measured from records on existing structures during free and forced vibration tests [24,25], but are typically calibrated through analytical expressions referred to rigid massless foundations, more or less embedded in the soil. The latter is generally assumed to be an elastic homogeneous half-space [23,26], an elastic stratum placed on a half-space (e.g. [23]), or a layered soil profile (e.g. [27]).

Under moderate to strong earthquake motions, the nonlinear and dissipative soil behavior modifies the impedance. Such a variation can be considered through the equivalent-linear approach [28], i.e. by estimating the variation of stiffness and damping from free-field site response analyses, or directly estimated through experimentally-based correlations with the foundation motion amplitude [29]. To overcome such a limitation, macro-element approaches can be adopted. In these approaches the overall soil-foundation behavior is reproduced by a single constitutive relationship, capable of describing the nonlinear behavior until failure [30,31].

Starting from the pioneering work by Veletsos and Meek [32] until the most recent analytical developments [33] and adaptations to non-trivial soil-foundation-structure systems (e.g. [34,35]), the simple oscillator with compliant base (Fig. 2a) represents the system most extensively adopted in engineering applications. Basically, it can be considered a reference elementary model to derive simplified approaches to calculate the SFS dynamic period and damping ratio (T^*, ξ^*), hence to obtain the modified inertial actions transmitted to the structure from the soil-foundation system.

Depending on the degree of coupling among the different SFSI mechanisms, the study of interaction effects through the models sketched in Fig. 2 can be handled by two kinds of analytical procedures:

- uncoupled approaches, in which the system is analyzed by decoupling the 'kinematic' from the 'inertial' interaction mechanisms with the so-called "sub-structure method";
- coupled approaches, i.e. "direct methods" by which all the interaction mechanisms can be evaluated simultaneously, performing dynamic analyses on a complete model including soil, foundation and structure.

In the first kind of procedures, i.e. by the "sub-structure method", a dynamic analysis is performed on a subsoil model which includes the foundation stiffness but neglects the structural mass. The resulting 'foundation input motion' (FIM) is used as dynamic loading of a compliant-base structural model, in which the soil-foundation system is replaced by a set of springs and dashpots. If the foundation is shallow, the kinematic interaction is negligible, hence the FIM is about coincident with the 'free-field motion' resulting from a conventional seismic response analysis. This approach is typically applied to the models shown in Fig. 2a-b-c.

Conversely, the coupled procedures jointly analyze the structure, the foundation and the subsoil, with this latter modeled as a continuum (see Fig. 2 d-e-f). In such cases, a rigorous calibration of all the parameters involved in the simulation is needed; otherwise, less realistic results may be obtained. On the other hand, in the uncoupled approaches an accurate definition of equivalent properties is mandatory to reliably account for material nonlinearity and the actual geometry of the single elements of the SFS system (i.e. structure with distributed mass, embedded and/or flexible foundation, soil inhomogeneity and/or irregular subsurface morphology).

Some aspects of the uncoupled approaches still represent a significant limitation in seismic performance assessment of URM structures, like:

(i) the transformation of a complex structure with diffused mass and stiffness into a SDOF system, and the consequent definition of the effective lumped parameters (inertia mass and flexural stiffness) associated with the fundamental mode of vibration of the fixed-base structure;
(ii) the difficult issue of modelling the building-soil interface considering the presence of underground stories or embedded foundations, which cannot be assumed as rigid structural elements tightly connected to the surrounding soil, due to the material nature and deterioration caused by aging.

It follows that, in principle, refined coupled procedures should be adopted for most URM structures, but the corresponding experimental and analytical effort can be justified only for high-value historical buildings. For ordinary residential structures, however, numerical simulations in which the SFS system is considered as a coupled model can support the calibration and validation of simpler and more sustainable approaches, as shown in the following sections.

3. Analyzed soil–foundation–structure systems

Fig. 3 summarizes the reference SFS models analyzed in this study. As in previous parametric studies [34], the structural geometry reproduces the transverse section of a residential masonry building with single-span floors. The width, b, and inter-story height are constant and respectively equal to 8 m and 4 m; the total height, h, varies considering 2 and 4 above-ground stories, which correspond to aspect ratios, h/b, equal to 1 and 2 (Fig. 3a). Such structural configurations are recurrent in constructions located in the Euro-Mediterranean region [21,36].

The structure consists of two load-bearing masonry walls connected each other by mixed floor systems, pinned to the walls and composed of steel I-beams, clay tiles and poor filling material. The sloping roof is made of timber elements. The thickness of the walls was assumed to vary along the building height, according to design practice rules adopted in the past for ancient masonry buildings (see [36]). In the case of two-story building, the wall thickness was set to 0.75 m at every story. Instead, in the case of four-story building, the thickness was set 0.75 m at the first two stories and 0.50 m at the last two stories.

As typical for masonry residential buildings [36], the embedded foundations were assumed to be constituted by the same material of the above-ground walls, with a width, B, and a depth, D, equal to 2.0 m and 2.5 m, respectively. The width was inferred from the empirical construction rules detailed in [36], while the depth was set so that the ratio D/B is close to unity, consistently with the definition of shallow foundations given by [37].

Fig. 3b shows the material types assumed for the load-bearing walls in this study: tuff stone masonry (TSM), rubble stone masonry (RSM), and clay brick masonry (CBM). These three types of masonry were selected as being the most recurrent in the Mediterranean area: the tuff stone is the construction material most widely used in volcanic and coastal plain environments; the rubble stone is usually adopted along the Apennine chain in Italy as well as in other countries in Eastern Europe; the clay brick masonry is widespread throughout the whole area.

The above building schemes were settled on a limited number of representative subsoil models, which were defined following the parametric studies described by [34,38]. The layerings, lithologies and mechanical properties of the selected subsoil models were assigned to reproduce realistic soil profiles conforming, on the average, to the

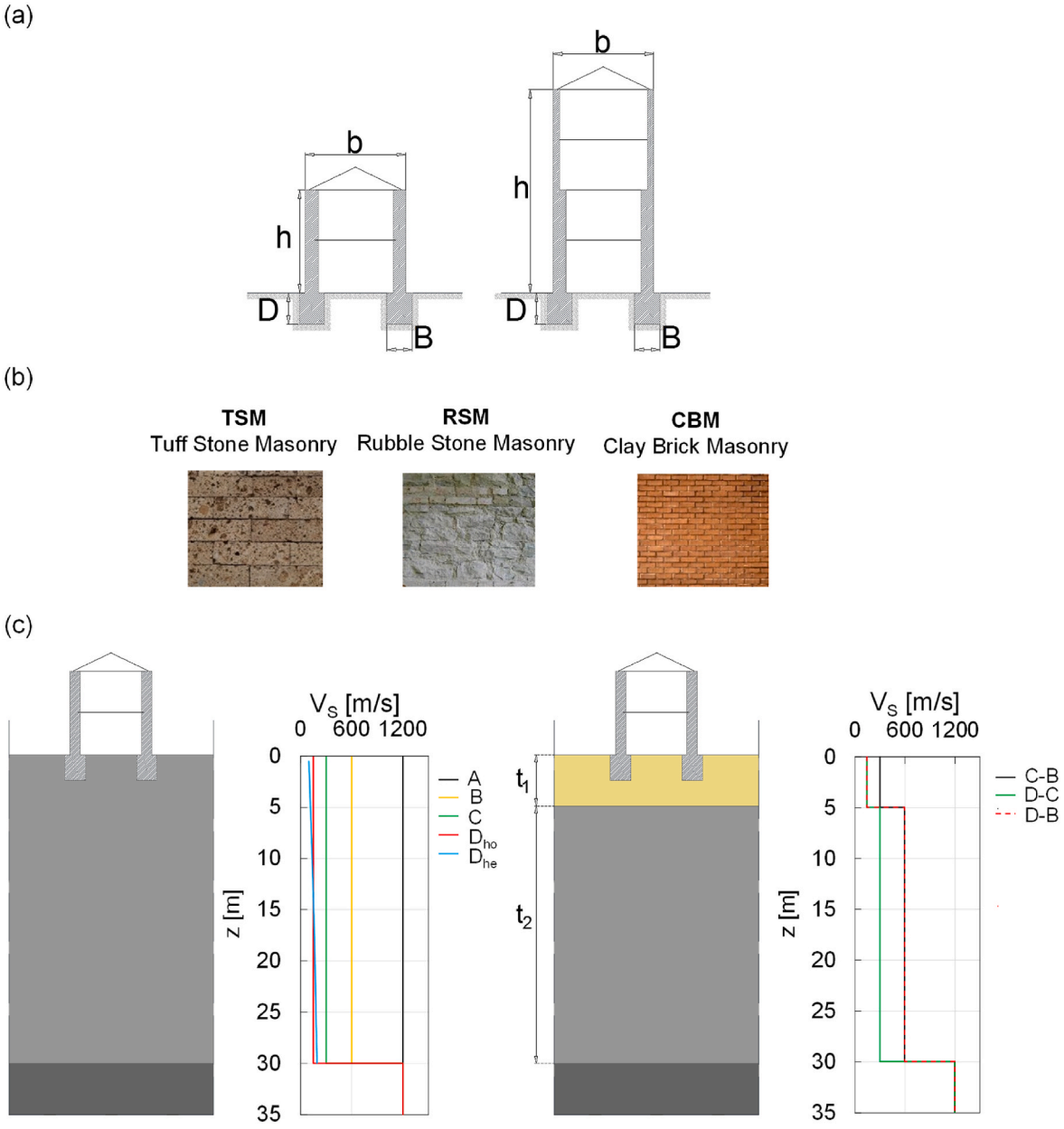

Fig. 3. (a) Structural configurations, (b) pictures of the masonry types, and (c) subsoil profiles analyzed in this study.

Eurocode 8 (EC8) ground type classification [39] and which can be frequently encountered in Mediterranean countries. In detail, the subsoil layerings consisted of:

- four homogeneous subsoil models, with lithology and properties representative of the EC8-conforming ground types A, B, C and D [39];
- three-layered subsoil profiles, D-B, D-C and C–B, constituted by a shallow cover with thickness $t_1 = 5$ m overlying a main formation as thick as $t_2 = 25$ m. Such subsoil configurations, which are typical in the Mediterranean area, maximize the stratigraphic site amplification, being associated with high impedance contrasts. The foundations are floating in the shallow cover, which maximizes the SFSI effects, due to the low soil-to-structure relative stiffness.

A stiff bedrock formation pertaining to ground type A was systematically assumed at a depth of 30 m. The shear wave velocity of soil types B, C and D was assigned as the mean value of the range pertaining to the relevant category defined by [39]. Subsoil model D is expected to mobilize the strongest SFSI effects, being characterized by the lowest stiffness. For this reason, its shear wave velocity was assumed as either constant (homogeneous profile, D_{ho}) or variable with depth (heterogeneous profile, D_{he}). The increase with depth of the shear stiffness at small strains, G_0, was described by a parabolic law, which was corrected with a linear trend close to the surface so that an unrealistic approach to zero was avoided, as assumed by Capatti et al. [40]. In the layered subsoil model, the shear stiffness of the D-type soil was set equal to that of the homogeneous profile, D_{ho}, because its variation in 5 m is not expected to be as significant as in thicker layers. The shear wave velocity profiles for the homogeneous and layered soil models are respectively shown in Fig. 3c.

Tables 1 and 2 summarize the material properties adopted in the linear and nonlinear analyses, respectively. Both soil and masonry were modeled as continuum materials with mass density, ρ, bulk modulus, K, shear modulus, G, and Poisson's ratio, ν. Floors and roof were modeled as equivalent beam elements made of a homogenized material.

Table 1
Material properties adopted for linear analyses.

Material	V_S (m/s)	ρ (kg/m^3)	K (MPa)	G (MPa)	ν
Soil A – bedrock	1200	2200	4224	3170	0.20
Soil B – gravel	600	2000	1200	720	0.25
Soil C – dense sand	300	1800	351	162	0.30
Soil D – loose sand	150	1600	108	36	0.35
TSM	–	1600	–	360	0.49
Steel-tile floor	–	1750	–	12,500	0.20
Timber roof	–	300	–	542	0.20

To carry out linear analyses (see Table 1), the soil density and Poisson's ratio were realistically assumed as respectively increasing and decreasing with V_S, and representative of soft rock (A), gravel (B), dense sand (C) and loose sand (D). The values of density were assigned as similar to those assumed in one-dimensional seismic response analyses reported in the parametric studies taken as references for the soil profiles ([34,38,40]). The values of Poisson's ratio (0.20, 0.25, 0.30, 0.35) reported in Table 1 were assumed as corresponding to typical mean values of the ratio V_P/V_S between compression and shear wave velocities, measured on rock, gravel, dense and loose sand, respectively. The properties of tuff stone masonry were defined from the experimental results collected by [41].

In nonlinear analyses (see Table 2), a limit shear strength was introduced for soil through a Mohr-Coulomb criterion with a friction angle, φ, which was respectively set equal to 40° and 35° for the coarse-grained formations associated with ground types B and C. A clayey soil was instead considered for ground type D profiles, which were assumed as characterized by an undrained strength, c_u, according to the Tresca criterion. The homogeneous and heterogeneous soil profiles, D_{ho} and D_{he}, were defined as representative of a lightly overconsolidated (o.c. in Table 2) and a normally consolidated (n.c.) clay, respectively, with a plasticity index $IP = 30\%$ for the homogeneous profile (D_{ho}) and $IP = 20\%$ for the heterogeneous profile (D_{he}). The variations of undrained strength with depth in the heterogeneous soil profile follow the assumptions adopted by Capatti et al. [40], namely, the existence of a crust with higher undrained strength was assumed in the shallowest 5 m. Due to the light overconsolidation, the undrained strength of the soil profile D_{ho} was set constant with depth and higher than that of the heterogeneous soil profile.

For all the analyzed soil profiles, a pre-failure hysteretic behavior was modeled as depicted in Fig. 4. The strain-dependent variation of normalized shear modulus, G/G_0, and the damping ratio, D, was described:

- for soil type B, by the standard curves reported by Stokoe et al. [42];
- for soil type C, by the curves suggested by Seed and Idriss [43];
- for soil profiles D, by the curves reported by Vucetic and Dobry [44] for the relevant plasticity indexes.

The standard curves were implemented in the numerical model by fitting them through 'sigmoidal' functions.

In nonlinear analyses, the energy dissipation at very small strains was simulated through a single-frequency Rayleigh approach, by assuming a minimum value of the damping ratio, D_0, ranging between 0.50% and 2% depending on the different soil type, and equal to the 5%

Table 2
Material properties adopted for nonlinear analyses.

Material	V_S (m/s)	ρ (kg/m^3)	K (MPa)	G (MPa)	ν	c_u (kPa)	φ (°)	c (MPa)	σ_c (MPa)	σ_t (MPa)	D_0 %
Soil A - bedrock	1200	2200	4224	3170	0.20	–	–	–	–	–	1
Soil B - gravel	600	2000	1200	720	0.25	–	40	–	–	–	0.60
Soil C - dense sand	300	1800	351	162	0.30	–	35	–	–	–	0.50
Soil D_{ho} - o.c. clay	150	1600	1788	36	0.49	100	–	–	–	–	2
Soil D_{he} - n.c. clay	100	1600	915	18	0.49	10	–	–	–	–	2
	191		2970	60		70					
RSM	–	1900	14,500	290	0.49	–	27	0.45	1.5	0.15	5
CBM	–	1600	25,000	500	0.49	–	36	0.87	3.5	0.35	5
Steel-tile floor	–	1350	30,000	12,500	0.20	–	–	–	–	–	–
Timber roof	–	300	1300	542	0.20	–	–	–	–	–	–

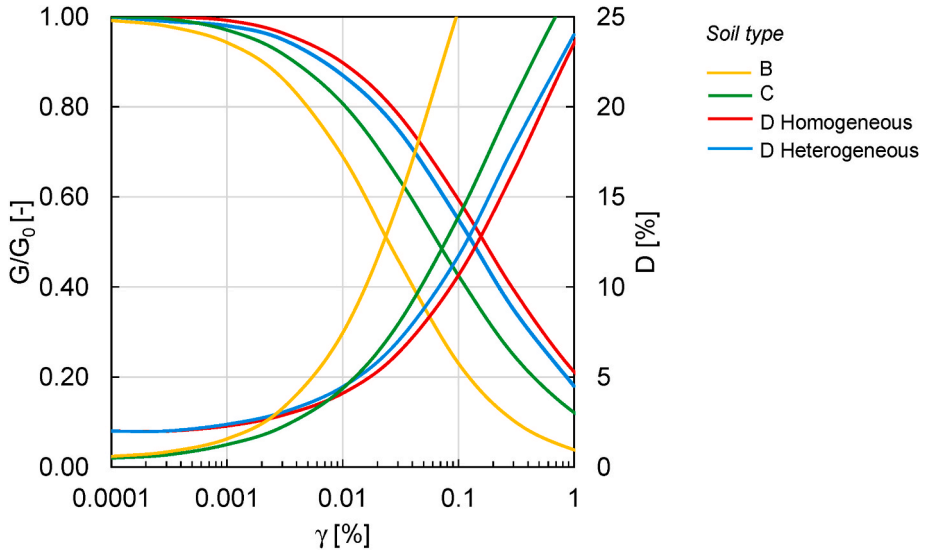

Fig. 4. Strain-dependent variation of normalized shear modulus and damping ratio assumed for nonlinear analyses.

conventional value for load-bearing masonry walls. The control frequency was calibrated by combining the fundamental frequency of the input motion with those of the *free-field* soil response and of the fixed-base structure, as detailed by Piro [45].

Linear analyses were focused on the masonry type characterized by average mechanical properties (i.e. TSM) and extended to all subsoil profiles considered. On the other hand, the nonlinear simulations were addressed to evaluate SFSI effects considering the most versus less deformable masonry types, i.e. clay brick masonry (CBM) versus rubble stone masonry (RSM). The masonry was modeled as an equivalent homogeneous material, by adopting an elastic-perfectly plastic constitutive model characterized by the Mohr-Coulomb failure criterion to limit the computational effort. The elastic parameters listed in Table 2 were set equal to the median values reported by the Italian Building Code Commentary [46] for existing masonry buildings. By contrast, the values of the strength parameters (friction angle, φ, and cohesion, c) reported in Table 2 were respectively set based on the friction coefficient, μ_s, and the Mohr-Coulomb criterion, by the following procedure.

Firstly, the value of μ_s was computed according to the expression [36]:

$$\mu_s = \frac{0.17}{\sqrt[3]{\sigma_0/\sigma_c}} \tag{2}$$

by assuming two values of σ_0/σ_c, respectively equal to:

- the ratio between the average compression stress, σ_0, at the base of the above-ground structure under the static loads, and the compression strength, σ_c, equal to the value reported in the Annex of the Italian Building Code [46];
- $\sigma_0/\sigma_c = 1/3$, which is the typical stress level suggested by the above code for the computation of the secant elastic modulus.

As a result, the average value of μ_s among those computed as above correspond to the tangent of the friction angle, φ, reported in Table 2.

The cohesion, c, instead, was back-calculated based on the Mohr-Coulomb criterion. Assuming the compression strength to be positive, the shear failure envelope in the σ_1-σ_3 plane can be expressed as follows:

$$\sigma_1 = k_p\sigma_3 + 2c\sqrt{k_p} \tag{3}$$

where σ_1 and σ_3 are, respectively, the principal maximum and minimum stresses; k_p is the coefficient of passive earth pressure, equal to:

$$k_p = \frac{1+\sin\varphi}{1-\sin\varphi} \tag{4}$$

By setting σ_3 equal to zero and σ_1 equal to σ_c, consistently with the uniaxial compression tests, the cohesion, c, can be computed as follows:

$$c = \frac{\sigma_c}{2\sqrt{k_p}} \tag{5}$$

A tensile cut-off, σ_t, equal to $0.1\sigma_c$ was also assumed in the masonry constitutive model.

Table 3 summarizes all the combinations of soil and structure models with the corresponding analyses represented by different color shadings.

4. Prediction of the fundamental frequency and damping of the SFS system

4.1. Coupled approach

The analyses listed in Table 3 were executed on continuum coupled models (see Fig. 2f) generated in the 2D finite difference code FLAC ver. 7.0 [47]. Fig. 5 shows the numerical model for the squat structure (slenderness ratio $h/b = 1$), as an example. The soil layering above the bedrock is 30 m deep and 50 mwide. The lateral extension of the main-grid domain on each side of the structure is higher than 2.5 times the building width, which is equal to 8 m for all the analyzed structural schemes. The vertical sides are restrained through the *free-field* boundary conditions, simulating an ideal horizontally layered soil profile connected to the main-grid domain through viscous dashpots. The soil rests on a 10 m thick layer simulating the bedrock, which was restrained at its bottom through dashpots oriented along the normal and shear directions, to simulate a half-space. The input motions were applied as shear stress time-histories to the bottom nodes of the grid.

The soil mesh consists of four-sided elements with the same arrangement for all the subsoil models. The element spacing was calibrated to respect the rule by Kuhlemeyer and Lysmer [48], so that input frequencies up to 25 Hz could be reliably propagated throughout the most deformable soil D. The soil mesh was densified in the central zone of the model, where the structural model is set. The load-bearing walls of the structure were modeled as a continuum, with the mesh spacing approximating the typical geometric dimensions of the masonry bricks. The thickness of load-bearing walls was reduced from 0.75 m to 0.50 m from the basement to the top of the very slender structure (see Fig. 3a). Conversely, the wall thickness was kept constant and equal to 0.75 m for the squat structure (see Figs. 3a and 5). One-dimensional beam elements were set along the height of the structural model, i.e. one on the roof and the others where the floors are located. The beam elements were linked to the load-bearing walls through pinned connections. The elastic properties of the beams are representative of 1 m-wide homogenized

Table 3
Summary of the dynamic analyses performed (linear: light blue; linear and nonlinear: red).

Soil model	Squat structure (h/b=1)			Very slender structure (h/b=2)		
	TSM	RSM	CBM	TSM	RSM	CBM
A						
B						
C						
D_{ho}						
D_{he}						
D-B						
D-C						
C-B						

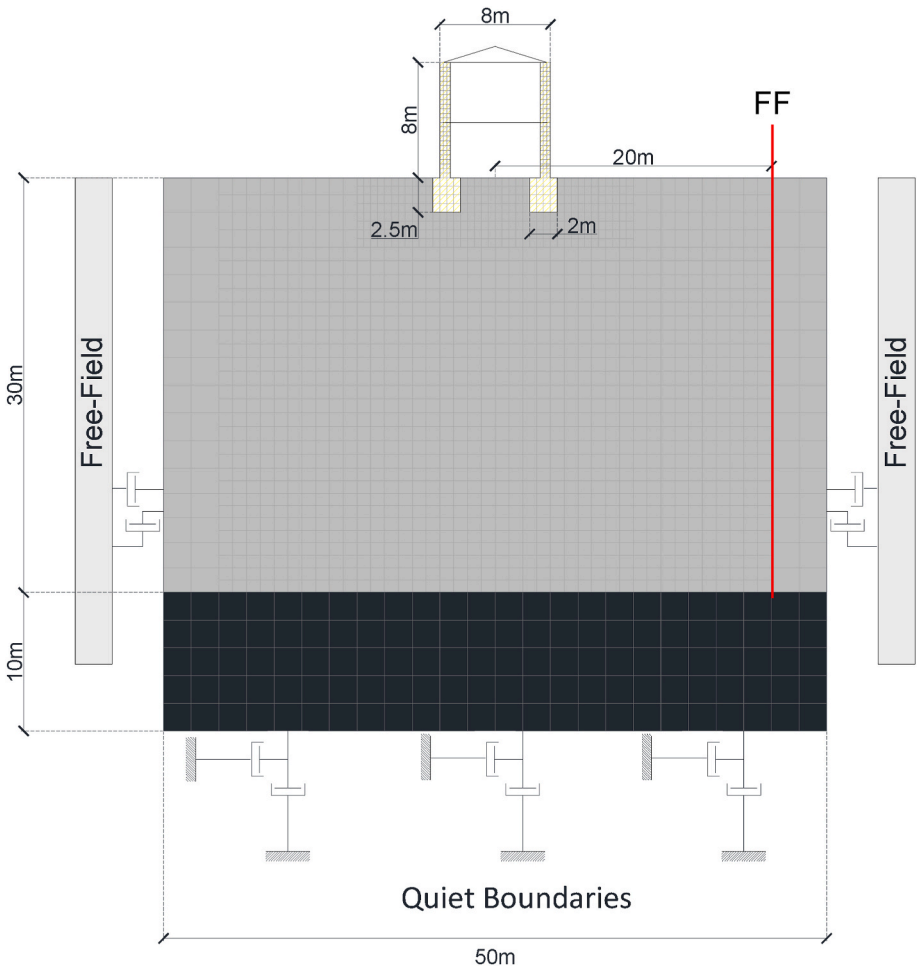

Fig. 5. Numerical model of the soil-foundation-structure system generated by FLAC software for the squat structural configuration.

cross-section of mixed steel-tile floor systems.

The predominant frequency of each free-field soil model at small strain level was firstly computed by assigning the linear properties listed in Table 1. A Rayleigh damping ratio as low as 0.1% was assigned in order to isolate the effect of the radiation damping. A linear visco-elastic analysis was performed under the random noise input motion shown in Fig. 6 in terms of acceleration time history (a) and Fourier spectrum (b). The resulting amplification functions plotted in Fig. 6c show peaks at a frequency of 10 Hz, 5 Hz, 2.5 Hz and 1.25 Hz respectively for the subsoil models A, B, C and D_{ho}. The latter are equal to the theoretical predominant frequencies of a homogeneous layer of the same thickness [49,50].

The procedure developed by de Silva et al. [51] was then used to compute the fundamental frequency of each SFS system. The model was subjected to the same noise signal lasting 10 s and the structural response was numerically monitored over 20 s to record the free-vibration behaviour of the SFS system after the end of the forced-vibration stage. The fundamental frequency, f^*, of each SFS system was then evaluated as that corresponding to the peak amplitude of the Fourier spectrum of the roof displacement during the free-vibration stage.

The plots in Fig. 7a-b shows the time histories and the Fourier spectra of the top displacement of the two-story ($h/b = 1$) and four-story ($h/b = 2$) structures, respectively, laying on homogeneous soil A and layered soil D-B. The SFS fundamental frequency f^* corresponds to spectral peak and is indicated by the dashed line. The f^*-value resulting from the analysis on soil type A was assumed to be equal to the fundamental frequency of the fixed-base structural model, i.e. f_0.

The time histories of the free vibration response (from 10 s to 20 s) show a progressive amplitude reduction with the number of cycles, which was interpreted through the well-known logarithmic decrement method [34] to quantify the damping ratio. The resulting values (reported in the left plots in Fig. 7) can be assumed as equal to the soil radiation damping, ξ_{rad}, because the material damping was set very low on purpose. As expected, the radiation damping is higher for the squat structure on the softest soil type (see the left plot in Fig. 7a). For the same SFS system, the reduction of the fundamental frequency with respect to the fixed-base value is not negligible, i.e. 4.18 Hz versus 5.01 Hz (right plot in Fig. 7a). Being the inertial SFSI effects less important with the reduction of the structure-soil stiffness ratio [34,51], both radiation damping and fundamental frequency of the tallest structure are much less sensitive to the soil deformability (Fig. 7b).

Table 4 shows the frequency and damping ratio of all the analyzed models. As expected, again, the frequency reduces and the damping increases with the soil deformability. Both effects are generally more evident for the squat structure ($h/b = 1$) on homogeneous soil.

4.2. Simplified approaches

Section 2 highlighted that the simplest way to model the inertial SFSI effects of a building placed on soft soil through shallow footings (see Fig. 8a) is the compliant-base SDOF drawn in Fig. 8b. The dynamic response of such a system can be equated to that of a replacement fixed-base oscillator (Fig. 8c) to obtain closed-form solutions for evaluating the fundamental frequency, f^*, and the damping ratio, ξ^*, of the SFS system.

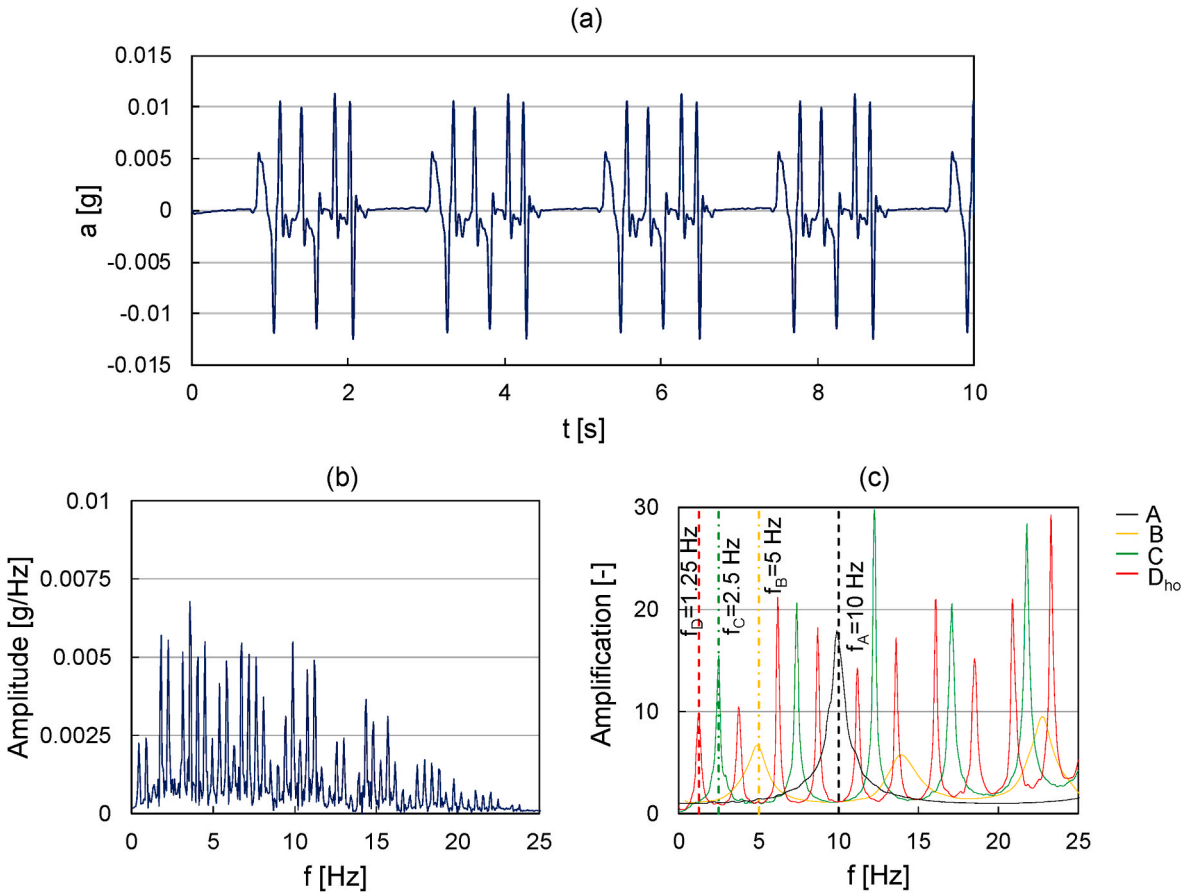

Fig. 6. Input noise for numerical dynamic identification of SFS systems: (a) acceleration time history; (b) Fourier spectrum and (c) amplification functions of the free-field homogeneous soil models.

As a matter of fact, Veletsos and Meek [32] derived f^* by exploiting the well-known expression of the fundamental frequency of the fixed-base SDOF, namely:

$$f^* = \frac{1}{2\pi}\sqrt{\frac{k^*}{m}} \tag{6}$$

where k^* results from the contributions of the structural flexibility and the foundation compliance relevant to both swaying and rocking motions, according to the following equation:

$$\frac{1}{k^*(f^*)} = \frac{1}{k} + \frac{1}{k_u(f^*)K_u} + \frac{h^2}{k_\theta(f^*)K_\theta r^2} \tag{7}$$

The second and the third denominators on the right side of Eq. (7) are the real parts of impedances of the whole building foundation associated with the horizontal translation and rocking modes. Specifically, the authors assume that the rotational impedance is given by the reaction of a vertical spring characterized by an arm equal to the radius, r, of a circle with the same area of the actual foundation. Alternatively, the rotational stiffness can be directly estimated through, for example, the Gazetas [52] formulas.

By substituting Eq. (7) into Eq. (6), the closed-form expression of the frequency reduction factor, f^*/f_0, was obtained as follows:

$$\frac{f^*}{f_0} = \frac{1}{\sqrt{\left[1 + \frac{k}{k_u(f^*)K_u}\left(1 + \frac{k_u(f^*)K_u}{k_\theta(f^*)K_\theta}\frac{h^2}{r^2}\right)\right]}} \tag{8}$$

The same authors equated the value of the pseudo-acceleration spectrum at f^* obtained from the response of the SFS system (Fig. 8b) and that of the replacement oscillator (Fig. 8c) to derive the following expression of the equivalent damping ratio:

$$\xi^* = \left(\frac{f^*}{f_0}\right)^3\left[\xi + \frac{(2-\nu)\pi^4\delta}{2\sigma^3}\left(\frac{c_u(f^*)}{k_u(f^*)[k_u(f^*)+ia_0c_u(f^*)]}\frac{r^2}{h^2} + \frac{c_\theta(f^*)}{k_u(f^*)[k_\theta(f^*)+ia_0c_\theta(f^*)]}\right)\right] \tag{9}$$

In Eq. (9), the parameter σ is the soil-structure relative stiffness defined as:

$$\sigma = \frac{V_S}{f_0\, h} \tag{10}$$

while the parameter δ is the structure-soil relative mass ratio:

$$\delta = \frac{m}{\rho\pi r^2 h} \tag{11}$$

The imaginary parts in Eq. (9) are negligible if $h/r > 2$. Predictions based upon Eq. (8) and Eq. (9) can be graphically expressed as a set of curves representing the dependence of f^*/f_0 on σ, as well as that of ξ^* on σ, given a specific value of δ.

It should be noted that Eq. (10) and Eq. (9) were derived under the hypothesis of a stiff massless footing resting on the surface of a homogeneous half-space. The consequent curves are hard to be applied to URM buildings with irregular geometry above and under the ground level, as well as with flexible foundations embedded in layered soil. To overcome such a limit, Piro et al. [34] proposed an approach to consider the contributions of the underground structural and foundation elements which can be significantly affected by the inertial interaction mechanism (see Fig. 9b). To this aim, the stiffness and the mass of each underground component are weighted through the corresponding areas

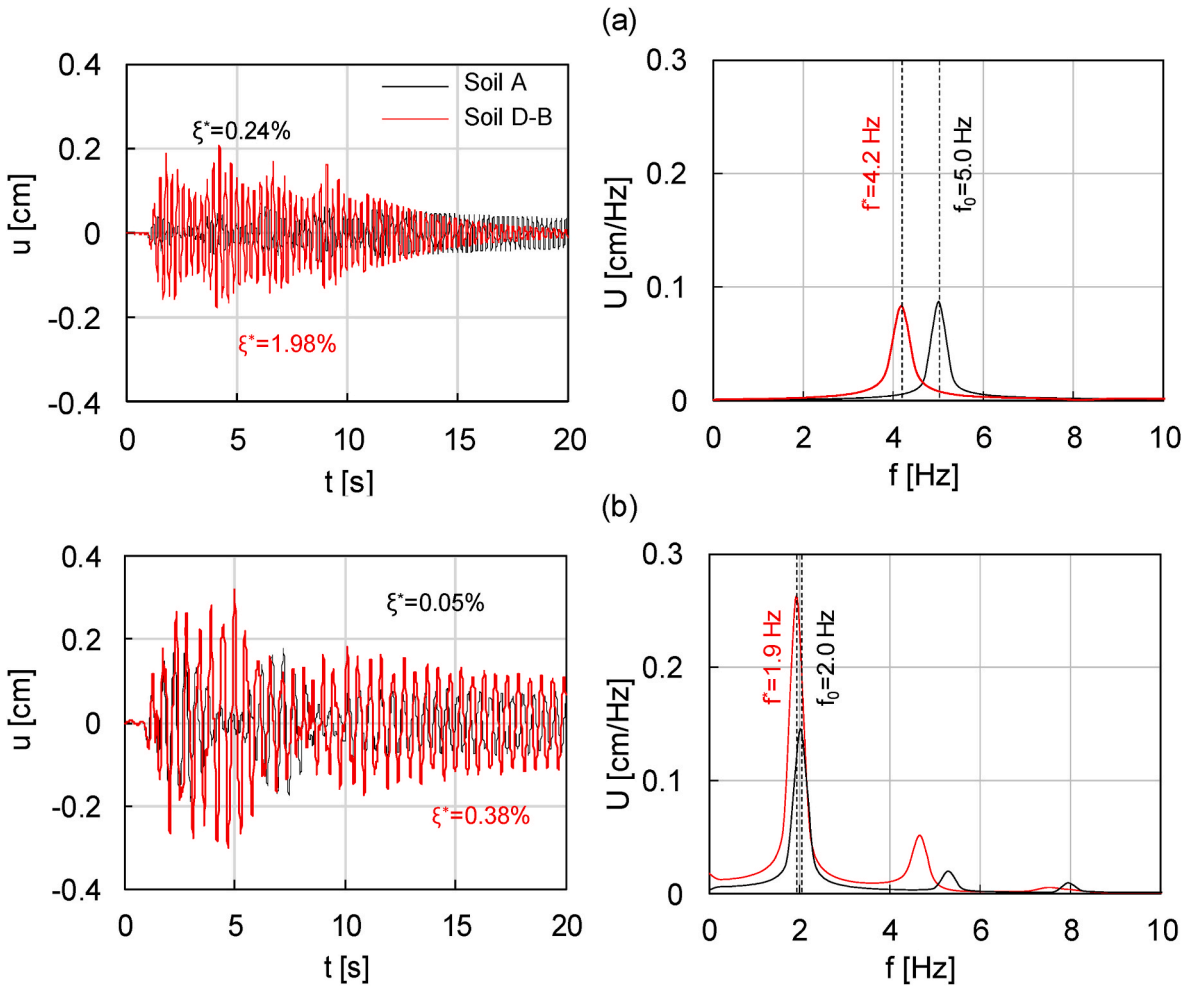

Fig. 7. Displacement time histories (left) and Fourier spectrum (right) at the top level for (a) two-story ($h/b = 1$) and (b) four-story ($h/b = 2$) TSM buildings on soil A (rock outcrop) and layered soil D-B.

Table 4
Frequency and damping ratio of the analyzed models.

Soil model	Squat structure ($h/b = 1$)		Very slender structure ($h/b = 2$)	
	f (Hz)	ξ (%)	f (Hz)	ξ (%)
A	5.01	0.24	2.02	0.05
B	4.92	0.99	2.02	0.22
C	4.64	3.36	1.97	1.08
D_{ho}	3.69	3.79	1.91	2.24
D-B	4.18	1.98	1.94	0.38
D-C	4.15	5.44	1.94	1.32
C–B	4.64	1.26	2.00	0.30

and through appropriately calibrated coefficients, to obtain an equivalent shear wave velocity, $V_{S,eq}$, that can be introduced in Eq. (10). The resulting value of the equivalent stiffness ratio:

$$\sigma_{eq} = \frac{V_{Seq}}{f_0\, h} \tag{12}$$

is then used to evaluate the frequency reduction factor, f^*/f_0, and the equivalent damping ratio, ξ^*, by referring to the same curves suggested by Veletsos and Meek [32], as shown in Fig. 9c.

As an example, the approach originally proposed by Veletsos and Meek [32] and its modification by Piro et al. [34] were applied to the SFS systems characterized by $h/b = 1$ and $h/b = 2$ on the layered soil profile D-B (see Fig. 7). Fig. 10 compares the results of both approaches in terms of frequency reduction (a) and increase of damping ratio (b) induced by the soil compliance. The horizontal dashed lines indicate the results of the numerical analyses for the two h/b ratios (see Fig. 7), assumed as benchmarks. It is apparent that the traditional formulation (hollow circles) excessively overestimates the frequency reduction and the damping ratio, if σ is calibrated on the V_S value of the shallow cover. Conversely, the procedure based on σ_{eq} (full circles) yields a frequency reduction factor in a very good agreement with the numerical analyses (Fig. 10a), and appears to significantly reduce the overestimation of the equivalent damping, even though still not enough for the case of squat structures (Fig. 10b).

4.3. Urban-scale application to the city of Matera

Fig. 11 shows the urban center of the historical city of Matera (Southern Italy) overlapped to a schematic geological map (Fig. 11a) and a representative stratigraphic section (Fig. 11b). The city is a UNESCO world heritage site, well-known for its peculiar 'Sassi' caves. The map and the section show that most of the center lies on the Sub-Apennine clays formation, the thickness of which varies from a few meters, near the Sassi area, to 40–50 m inwards. The clay deposit lays on the soft rock Gravina calcarenite formation, where the Sassi caves were excavated, which in turn overlies the stiff Altamura limestone, outcropping to the East of the city center.

Extensive measurements of shear wave velocity through down-hole and seismic refraction tests (see Fig. 11a) were carried out in Matera

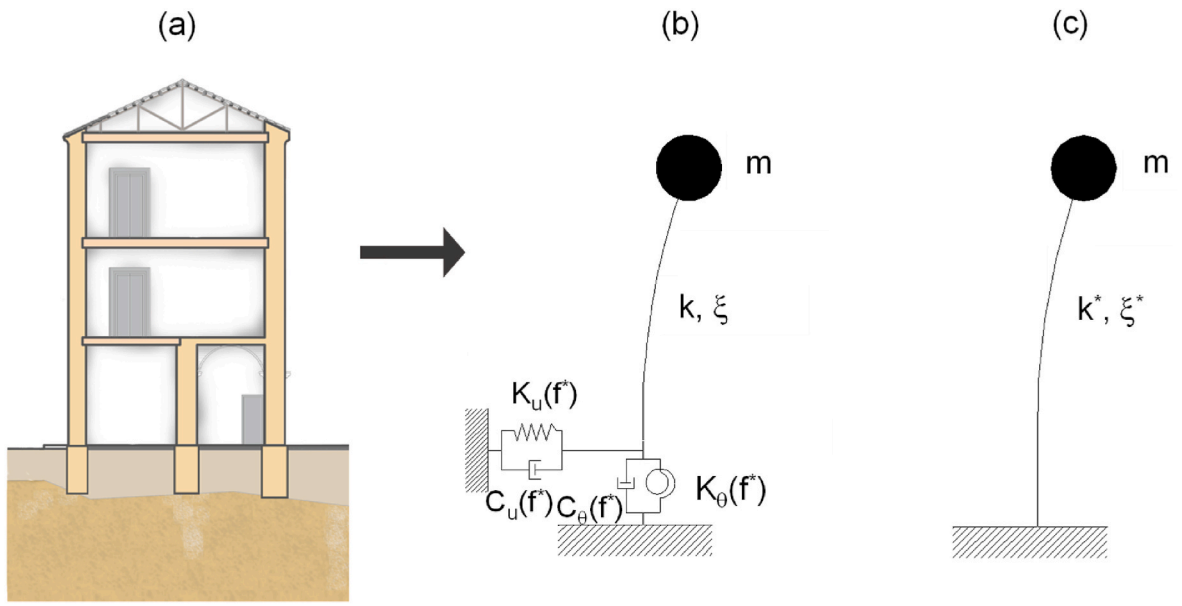

Fig. 8. (a) Typical transverse cross-section of an URM building, (b) the equivalent compliant-base SDOF system, and (c) the corresponding replacement oscillator.

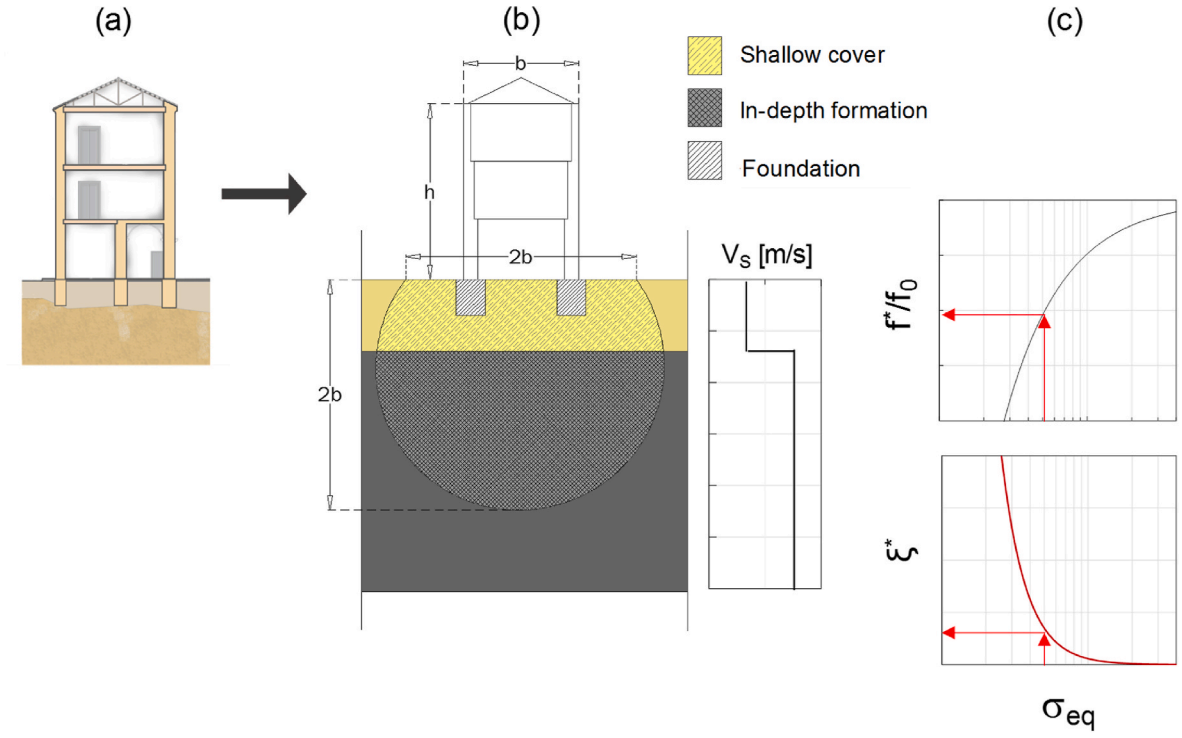

Fig. 9. Approach for the estimation of the frequency reduction factor, f^*/f_0, and equivalent damping ratio, ξ^*, of a SFS system: (a) typical transverse cross-section of an URM building; (b) soil volume affected by inertial interaction mechanism; (c) frequency reduction factor, f^*/f_0, and equivalent damping ratio, ξ^*, versus equivalent soil-structure stiffness ratio, σ_{eq}.

and collected in the CLARA WEBGIS (https://smartcities-matera-clara.imaa.cnr.it/). Those tests revealed that the shear wave velocity, V_S, of Sub-Apennine clays increases with depth from 146 m/s to 450 m/s. The values of V_S for the Gravina calcarenite range between 394 m/s and 1185 m/s, depending on its degree of cementation, while those measured in the Altamura limestone are much less variable and equal to 950 m/s on average.

During the CLARA project [53], the dynamic response under environmental noise of numerous buildings was recorded and analyzed through Horizontal/Vertical (H/V) spectral ratios to quantify their fundamental frequency. Gallipoli et al. [54] correlated the measured frequency with the building height to derive empirical predictive equations. The latter relationships were differentiated according to the underlying foundation soil, because the frequencies measured on buildings founded on the Sub-Apennines clays were lower with respect to those measured on those laying on the Gravina calcarenite, even when the structural features were found to be similar. Such difference suggests possible SFSI effects, caused by the low V_S – values of the Sub-Apennines

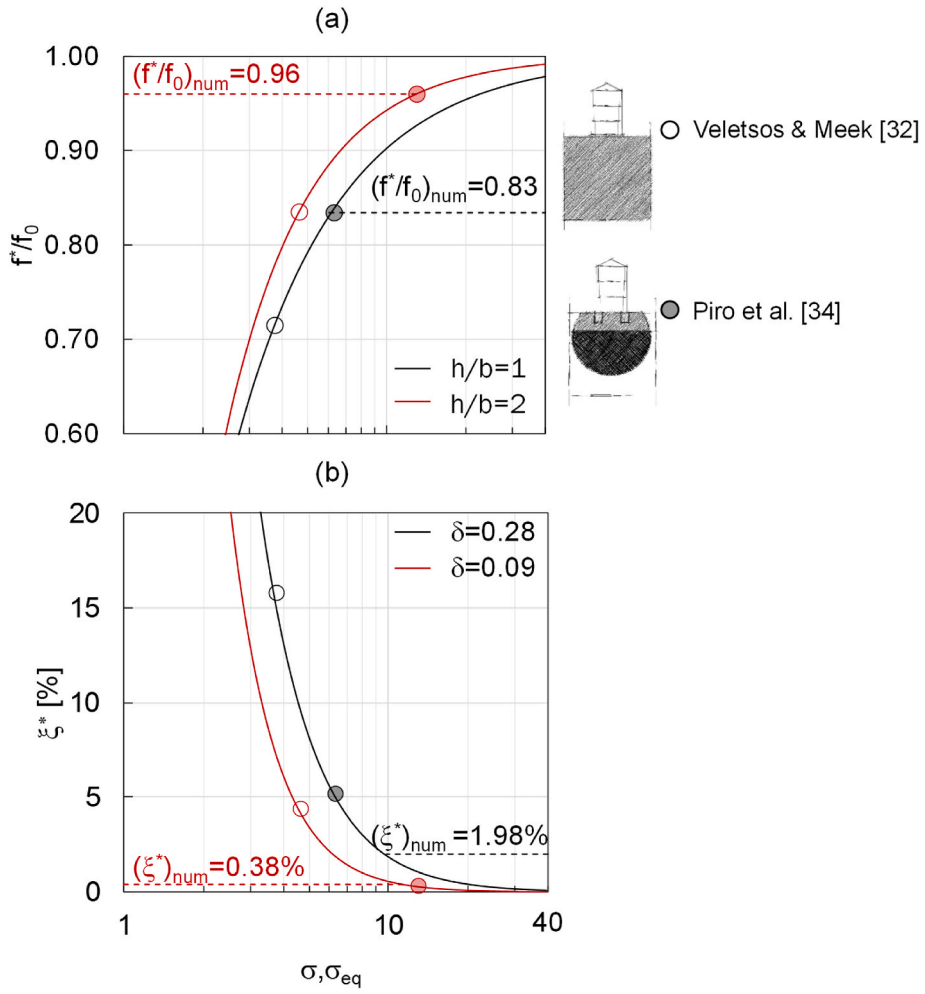

Fig. 10. Comparison between the frequency reduction (a) and radiation damping ratio (b) estimated through the approaches by Veletsos and Meek [32] and Piro et al. [34] for two and four-story SFS systems on layered soil profile D-B.

clays close to surface.

For this reason, the simplified approaches described in Section 4.2 were applied to the seven representative buildings localized in Fig. 11. Fig. 12 shows photos and schematic cross-sections of the analyzed soil-foundation-structure systems. The extensive survey by Gallipoli et al. [54] allowed for the determination of height, width and number of stories of the buildings. The thickness of the load-bearing walls was estimated by empirical correlations, hence assumed as enlarged by 0.15 m at each side from the ground floor down to a depth of 1.5 m, to define the geometrical features of masonry shallow foundations. The load-bearing walls and the foundations are made of calcarenite blocks with irregular texture, the mechanical properties of which were assigned according to the typical ranges suggested by the Italian Building Code Commentary [46], in lack of more accurate measurements.

For each building, the soil layering and the shear wave velocity profile were inferred from the closest available investigations (see Fig. 11a), as detailed in [55,56]. The unit weight was set equal to 17.50 kN/m^3, 19.50 kN/m^3 and 27.50 kN/m^3 for the clay, calcarenite and limestone formations, according to typical values.

The fixed-base fundamental frequency, f_0, was firstly estimated for each building through the empirical correlation proposed by Gallipoli et al. [54] for the buildings founded on calcarenite. The resulting values are compared to the fundamental frequency directly measured on the building, f^*_{exp}, in Fig. 12 and in Table 5. As expected, f^*_{exp} is always lower than f_0 and their ratio reduces with the thickness of the clay layer, even when the number of stories is the same (see, for instance, buildings 1, 2 and 5). This is a clear evidence of the influence of the variable subsoil conditions and of the related effect of SFS interaction on the building dynamic response.

Such influence was confirmed by the estimation of f^* through the analytical approaches. Table 5 reports the analytical values together with the reference shear wave velocity and soil-structure relative stiffness as for both simplified approaches discussed in section 4.2. A percentage error, ε, with respect to f^*_{exp} was computed as follows:

$$\varepsilon = \left(\frac{f^*_{\exp} - f^*}{f^*_{\exp}} \right) \times 100 \tag{13}$$

On average, the traditional formulation by Veletsos and Meek [32] overestimates the experimental fundamental frequency, while a better agreement was found when the approach by Piro et al. [34] was applied. The only exceptions are represented by buildings 5 and 7, which are hard to be well-approximated through simplified SDOF models, due to their hollow geometrical plan.

Fig. 13 graphically shows the comparison between the experimental frequencies and the predicted values, indicating the thickness of the Sub-Apennines clay with a marker size proportional to its value H_c. The plots clearly highlight that the approach proposed by Piro et al. [34] improves the match between the predicted and measured values, especially when the clay thickness is relatively lower, because it accounts for the stiffer deep layers.

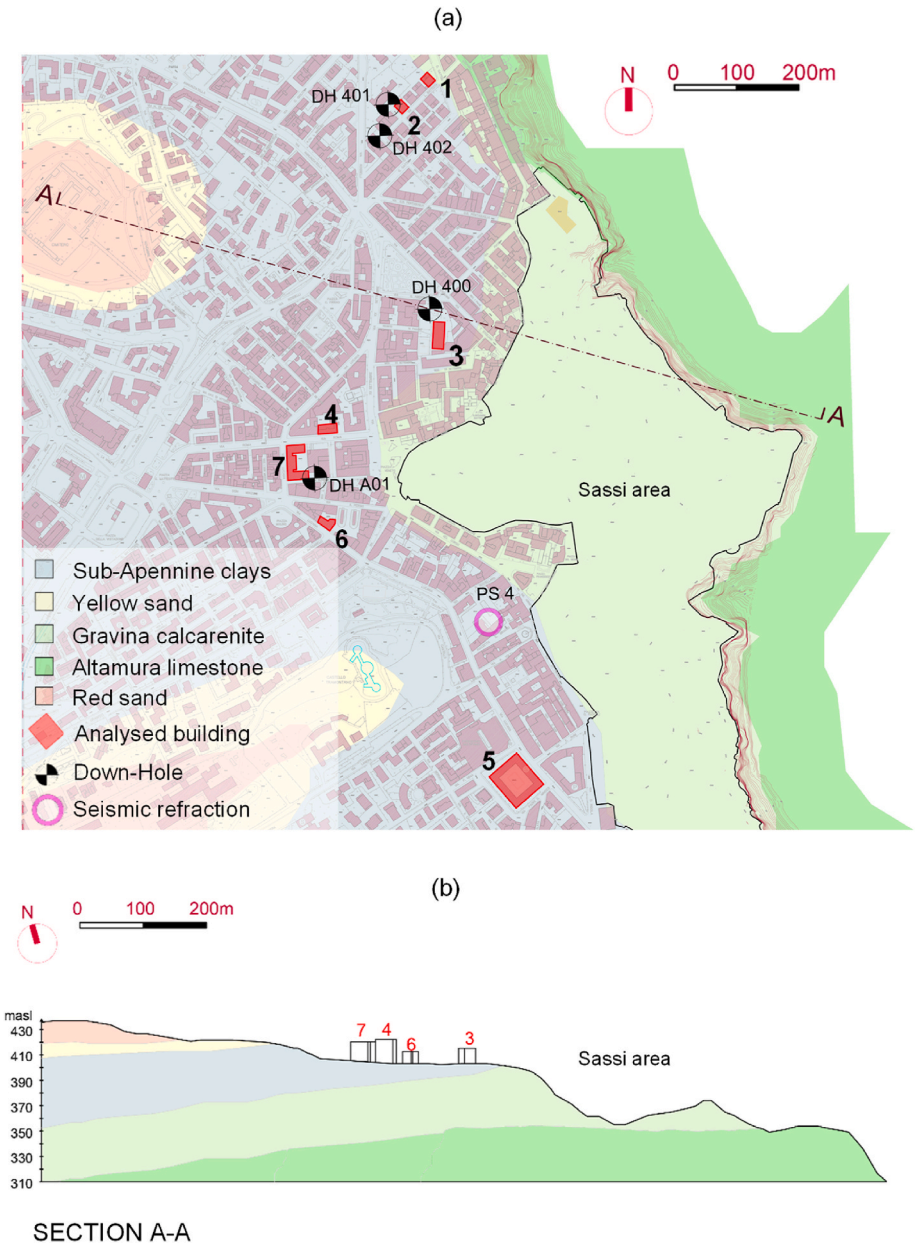

Fig. 11. (a) Geological map and (b) schematic section of Matera with the location of analyzed buildings.

5. Seismic performance, vulnerability, and damage of SFS systems under out-of-plane excitation

5.1. Reference input motions

A so-called 'cloud analysis' [57] of the SFS systems was carried out to investigate the impact of SFS interaction on seismic vulnerability of masonry walls to out-of-plane damage and plastic behavior of the soil-foundation system. Seismic performance of the SFS systems under study was analyzed via nonlinear time history analysis (NLTHA) [45].

A suite of reference input motions was sorted out from the SIMBAD database [58]. For each horizontal component (i.e., EW or NS) of the 467 ground motion records available therein, the spectral acceleration $S_a(T^*)$ was calculated. Thereafter, the ground motions were sorted in descending order of the geometric mean between the spectral accelerations associated with the two components. The suite of 15 natural ground motions reported in Table 4 was finally selected, by taking care that they are:

1) capable of producing a wide range of spectral accelerations, i.e. $S_a(T^*) = 0.01g$–$1.20g$;
2) recorded during different earthquakes;
3) recorded on stiff outcropping formations.

The last criterion was adopted because site effects were explicitly considered in the coupled SFS analysis. However, only 38 ground motions recorded on type A soil were available in the whole accelerometric database, and several of them were related to the same seismic events. Thus, the suite of 10 records on stiff rock outcrop was enriched with 5 high-amplitude signals recorded on type B soil with an equivalent shear wave velocity, V_{S30}, generally higher than 500 m/s.

Each record was applied as input motion to the base of the 16 coupled SFS models highlighted in Table 3 (see the red-hatched cells therein), the performance of which was analyzed using NLTHA.

Fig. 14a shows the acceleration time histories of the selected records, evidencing their different amplitudes, frequency content and duration over a 40-s time frame.

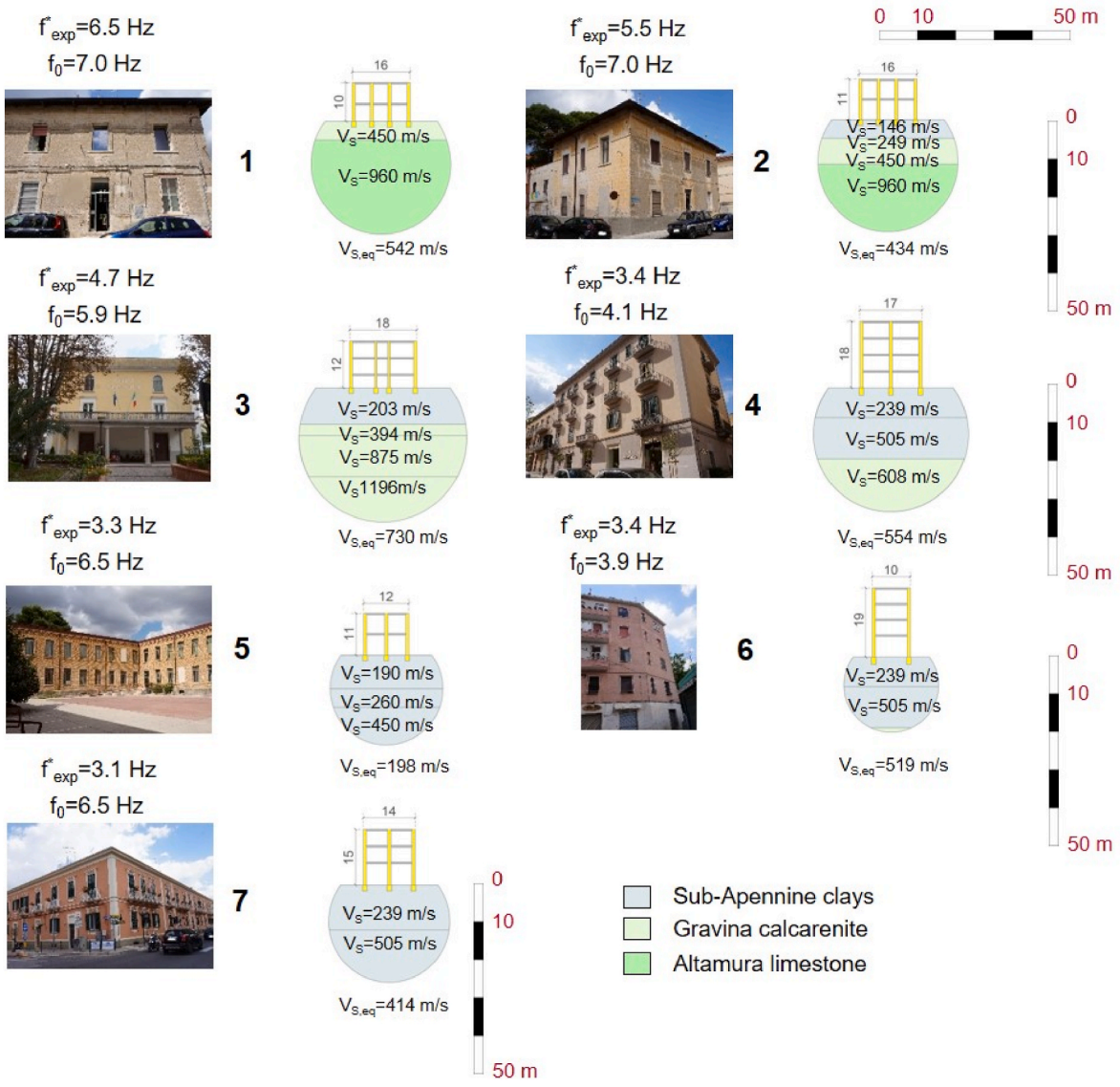

Fig. 12. Pictures of the analyzed buildings and reference schemes for the application of the simplified approach.

Table 5
Comparison between fixed-base (f_0) and compliant-base frequencies, as measured by H/V spectral ratios (f^*_{exp}) and predicted with the simplified approaches (f^*).

Building ID				Veletsos and Meek [32]				Piro et al. [34]			
	H_c (m)	f_0 (Hz)	f^*_{exp} (Hz)	V_S (m/s)	σ (−)	f^* (Hz)	ε (%)	$V_{S,eq}$ (m/s)	σ_{eq} (−)	f^* (Hz)	ε (%)
1	0	7.0	6.5	450	6.2	5.9	10.0	542	7.4	6.1	7.0
2	5	6.7	5.5	146	2.0	2.9	47.0	434	5.9	5.5	0.0
3	10	5.9	4.7	203	2.8	3.6	23.8	730	10.0	5.4	−14.4
4	19	4.1	3.4	239	3.3	3.0	12.0	554	7.6	3.8	−10.0
5	>24	6.5	3.3	190	2.6	3.8	−13.6	198	2.7	3.9	−17.2
6	19	3.9	3.4	239	3.3	2.9	15.0	519	7.1	3.6	−5.0
7	>26	4.9	3.1	239	3.3	3.3	−9.0	414	5.7	4.1	−33.0

The high variability of the selected input motions is further remarked in Fig. 14b, which shows the scatter plot of peak ground acceleration (PGA) versus moment magnitude (M_W) and epicentral distance (R), that respectively range in the intervals [0.06g, 1.15g], [5.2, 7.1] and [5.10 km, 28.57 km], as outlined in Table 6. Fig. 14c shows that there is more than one order-of-magnitude variation in spectral acceleration associated with the fundamental periods of the five different soil profiles, indicated by the vertical dashed lines.

5.2. Performance assessment of SFS components

As a basis for an in-depth analysis of SFS systems, soil amplification in free-field conditions was firstly investigated in terms of PGA and spectral ratios between foundation level and bedrock motions, which are respectively denoted as PGA_s/PGA_r and $S_{a,s}/S_{a,r}$ in Fig. 15a and b. Acceleration amplitudes and response spectra were derived from ground motion time histories predicted at the foundation level ($z = -2.5$ m) and 20 m far away from the building vertical axis, which was a distance

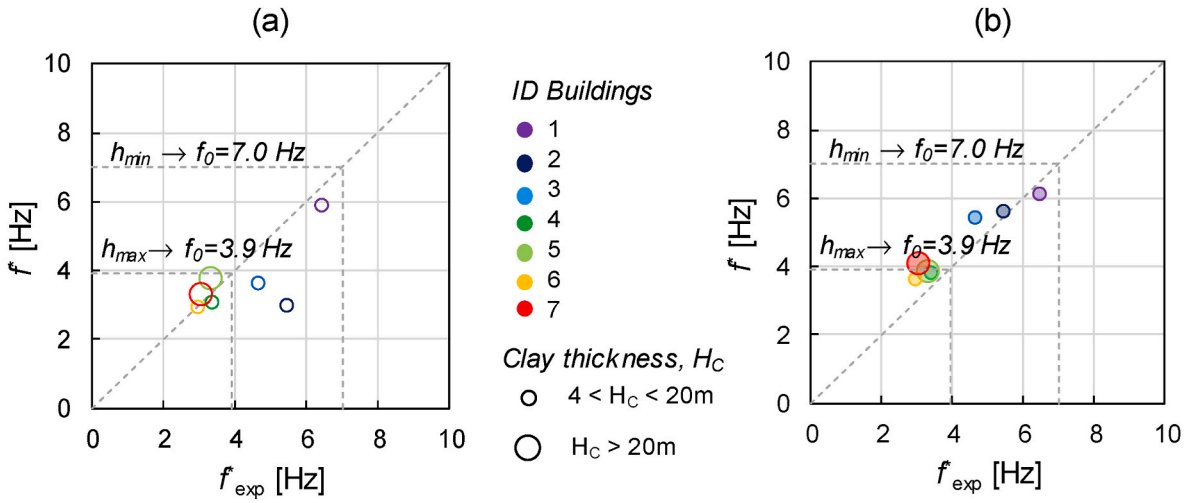

Fig. 13. Comparison between the experimental and analytical frequencies, the latter calculated with the (a) traditional [32] and (b) updated [34] approach.

assumed to be representative of free-field conditions (see Fig. 5).

In the first figure, the PGA_s/PGA_r ratio is plotted against PGA_r: the numerical ratios computed on soil types B, C and D (the latter considering homogeneous and heterogeneous soil profiles, D_{ho} and D_{he}) are compared to the mean curves (solid lines) describing the nonlinear amplification factors proposed by Tropeano et al. [38] for the reference soil types. In this case, these latter on the average appear fairly more conservative than the data points characterizing this study, which are referred to the foundation level rather than to surface.

Fig. 15b shows the comparison between spectral ratios relevant to both homogeneous and heterogeneous soft soil models, D_{ho} and D_{he}, as excited by ground motions #1, #8 and #14, which were respectively characterized by PGA_r values equal to 1.15*g*, 0.40*g* and 0.06*g*. Spectral ratios are plotted against the fixed-base vibration period. Red and black vertical lines respectively identify the ranges of fundamental vibration periods of clay brick and rubble masonry buildings, as numerically evaluated via structural models with either $h/b = 1$ or $h/b = 2$, assumed as with fixed-base or laying on a soft soil profile, either D_{ho} or D_{he}.

Due to the higher structural stiffness, the fundamental vibration period of CBM buildings is distinctly lower than that of the corresponding RSM models, and their difference increases with the aspect ratio h/b. The structural period elongation under increasing h/b consequently results into a significantly lower spectral acceleration, opposed to what is expected in terms of spectral displacement demand on the SFS system.

Under the strongest input motion #1, significant de-amplification of both *PGA* and spectral acceleration (resulting in $S_{a,s}/S_{a,r} < 1$) can be observed in the period range of the two-story buildings ($h/b = 1$) located on both soft soil profiles. By contrast, the highest amplification of spectral amplitudes is found under the weakest input motion #14 (resulting in $S_{a,s}/S_{a,r} > 1$), particularly in the case of heterogeneous soil model. A significant amplification of spectral acceleration is observed in the period range of four-story buildings ($h/b = 2$) over all three ground motions under consideration. This is apparent especially for the CBM slender structure, because of its fundamental period very close to that of the soft soil, especially when considering the case of the heterogeneous profile (compare Fig. 15b with Fig. 14b). Such condition can induce a 'double resonance' effect resulting by the dynamic coupling of the input motion with the soil, and of the soil with the structure.

To assess the seismic performance of the foundation system, the maximum settlement (w) and the tilting rotation (θ) were assumed as engineering demand parameters (EDPs), as illustrated in Fig. 16. Time histories of the settlements (w_1 and w_2) of the opposite corners of each footing were recorded during the analysis, allowing the calculation of θ as their difference ($w_1 - w_2$) divided by the foundation width (B).

For each of the analyzed cases, the reference value of both w and θ was assumed as the absolute maximum value attained during the time history, which can be considered as an over-estimate of the permanent value.

For each deformable soil type assumed in this study, Fig. 17 shows the values of the above-mentioned EDPs of CBM buildings with $h/b = 1$ (left column) and $h/b = 2$ (right column) under varying *PGA* at the bedrock. Maximum settlements of structures with $h/b = 2$ are visibly larger than those associated with $h/b = 1$, due to more pronounced rocking induced in the foundation soil by the heavier and taller four-story buildings (Fig. 17a-b). It is immediate to observe that assuming a homogeneous type D soil model may result into significantly lower settlement predictions: in fact, the lower stiffness and strength of type D_{he} soil profile close to the surface leads to higher foundation settlements than those resulting for the D_{ho} model. Nevertheless, for the squat structure (Fig. 17a) the settlements relevant to the stiffer C soil model result higher than those of the homogeneous D profile and, for two input motions, even of the heterogeneous one. This is an effect resulting from soil-building resonance, which can be justified by comparing the periods T_C in Fig. 14c and T^*_{CBM} in Fig. 15c. In any case, w-values predicted under even the highest *PGA*-values are below the conventional threshold levels adopted in engineering practice for assessing the damage of load-bearing masonry walls, which are typically set to approximately 2.5 cm [59].

Fig. 17c and d shows the values of θ predicted for each soil type and *PGA* level, confirming higher demand levels in case of heterogeneous soil type D compared to the homogeneous profile. Nonetheless, the difference between the maximum rotations are significantly smaller than those observed on settlements. Under some *PGA* levels, it is worth noting that assuming a homogeneous type D soil produces maximum rotations that are lower than those observed on type C soil. It is also noted that tilting rotation evaluated on the two-dimensional SFS systems under study, characterized by out-of-plane loaded masonry walls, can be viewed as representative of an overestimate of the in-plane shear deformation of orthogonal masonry walls, which would induce a constraint between two opposite walls in three-dimensional SFS models representative of the entire building. In all cases, even the maximum θ-values are below the typical thresholds associated with the in-plane shear failure of load-bearing masonry walls adopted in engineering practice, i.e. 1/200 = 0.5% [60].

The maximum interstory drift ratio (*MIDR*) was assumed as the engineering demand parameter EDP representative of the structural out-of-plane response. IDR_j is the ratio between the relative horizontal displacement of the j-th story ($\Delta u_{str,j}$) and interstory height (h_j), so *MIDR* was defined as follows:

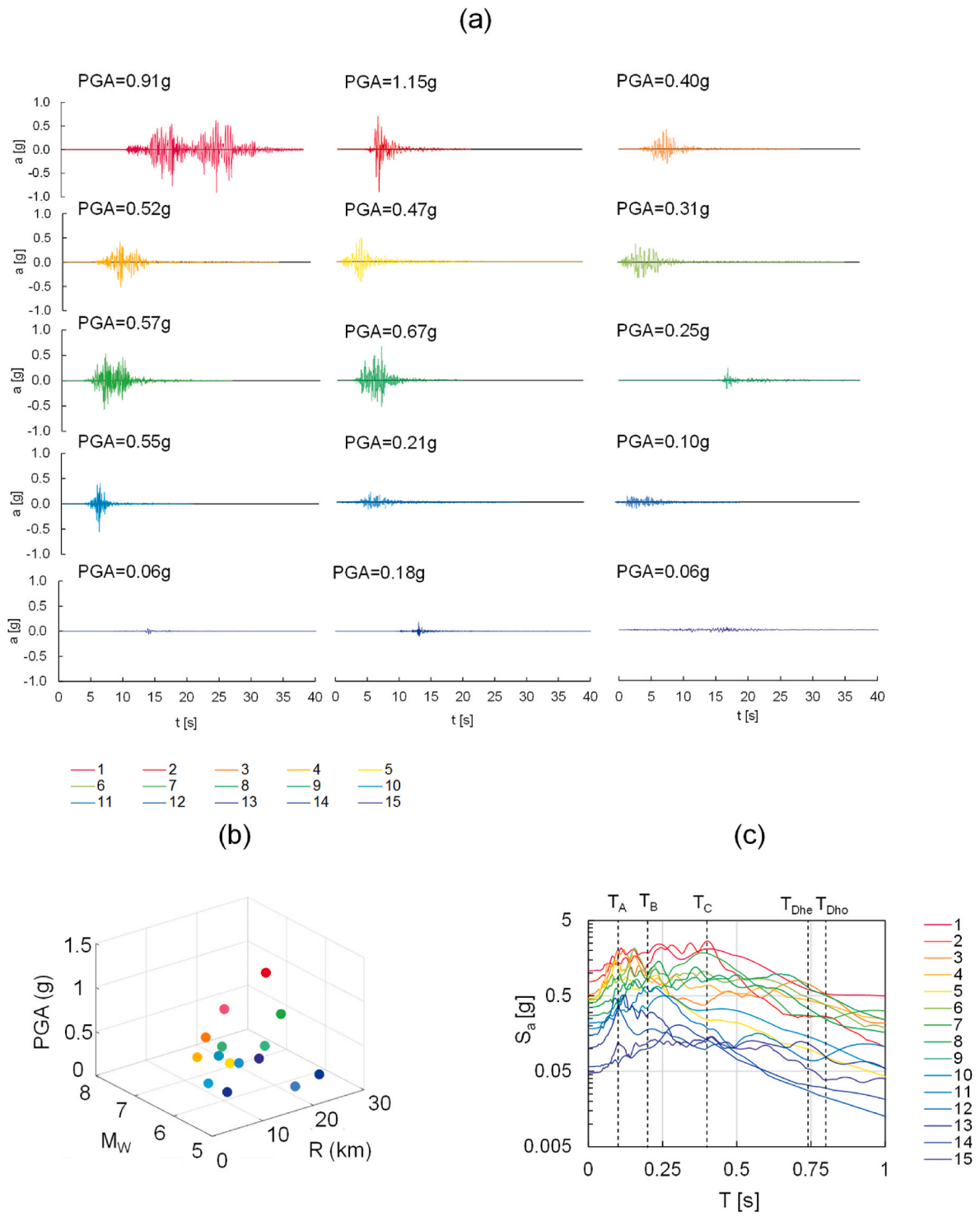

Fig. 14. Selected ground motion records: (a) accelerograms, (b) *PGA–M_W–R* scatter plot and (c) acceleration response spectra.

$$MIDR = \max\left\{\frac{u_{str,j} - u_{str,j-1}}{h_j}\right\}_{j=1,\ldots,N} \tag{14}$$

where $u_{str,j}$ and $u_{str,j-1}$ are the horizontal displacements of the j-th and j-th–1 floors, respectively. The structural horizontal displacements, u_{str}, were obtained as the total displacement amplitude minus that induced by the rigidbase motions corresponding to the foundation rotation and translation. The calculation was done in the time window preceding the spread of the plastic state in the whole resistant section at the base of the masonry wall.

The maximum value of interstory drift ratio (*MIDR*) was computed on numerical models that, for the sake of computational efficiency, do not allow for direct consideration of some mechanical phenomena associated with actual collapse, namely: (i) post-peak strain softening of masonry, (ii) loss of masonry integrity, and (iii) geometric nonlinearity due to large OOP displacements and rotations. This justifies why in some cases apparently large *MIDR*-values were attained. Nonetheless, no major effects on the accuracy of fragility curves are expected, because the occurrence of OOP damage levels under consideration is controlled through the adoption of realistic values of *MIDR*.

Table 6
Main characteristics of the selected ground motions.

#	ID [58]	Earthquake	Date	M_W	R (km)	Soil type	V_{S30} (m/s)	Component	PGA (g)
1	208	Duzce	12-11-1999	7.1	27.16	B	481	EW	0.91
2	47	Rumoi	14-12-2004	5.7	8.08	B	579	EW	1.15
3	217	Olfus	29-05-2008	6.3	8.89	A	/	NS	0.67
4	386	Christchurch	13-06-2011	6	5.10	A*	/	EW	0.57
5	357	Christchurch	22-02-2011	5.6	8.42	A*	/	NS	0.55
6	209	Bingol	01-05-2003	6.3	11.79	B	529	EW	0.52
7	452	Loma Prieta	18-10-1989	6.9	28.57	A	1428	NS	0.47
8	117	South Iceland	21-06-2000	6.4	12.15	B	/	EW	0.40
9	422	Friuli 1st S	06-05-1976	6.4	21.72	B	522	NS	0.31
10	216	Parkfield	28-09-2004	6	7.14	A	1340	EW	0.25
11	467	Kozani MS	13-05-1995	6.5	16.69	A	/	EW	0.21
12	109	Anza	12-06-2005	5.2	18.45	A	/	EW	0.18
13	430	Friuli 4th S	15-09-1976	5.9	10.04	A	901	NS	0.13
14	62	Kyushu	09-09-1996	5.7	27.04	A	889	NS	0.06
15	413	Irpinia	23-11-1980	6.9	23.77	A	1149	NS	0.06

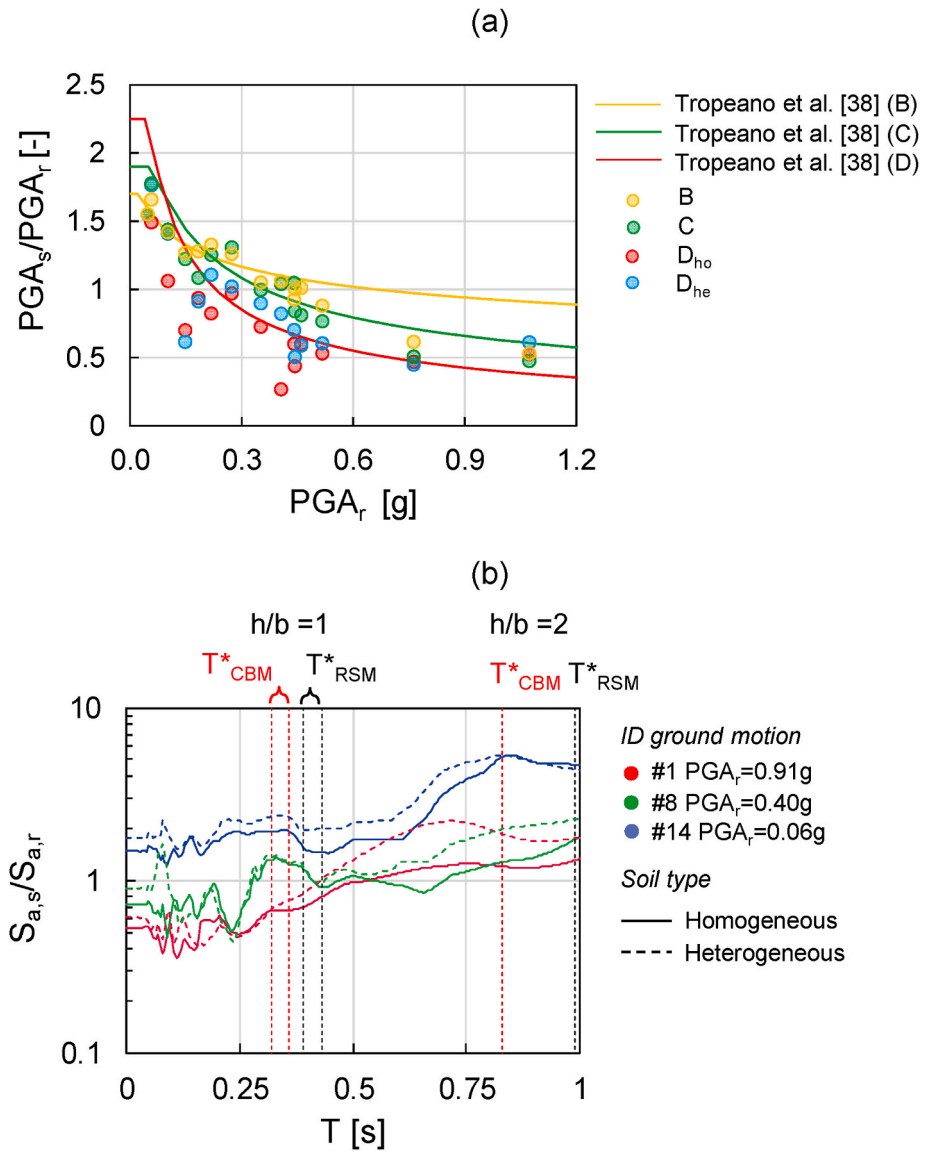

Fig. 15. (a) Ratios between free-field acceleration amplitude at the foundation level (PGA_s) and bedrock motion (PGA_r) for stiff to soft soil profiles, compared with the mean amplification factors reported by Tropeano et al. [38]; (b) spectral ratios between free-field motion at the foundation level ($S_{a,s}$) and bedrock motion ($S_{a,r}$) for soft soil D_{ho} and D_{he} profiles.

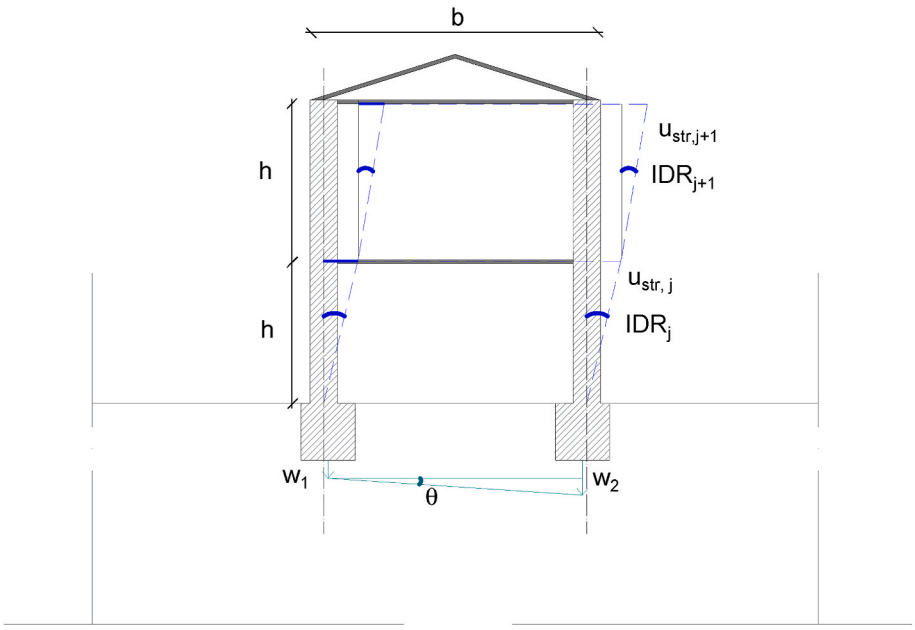

Fig. 16. Graphical definition of foundation settlements (w_1, w_2), tilting rotation (θ), and interstory drift ratio of the j-th story (IDR_j).

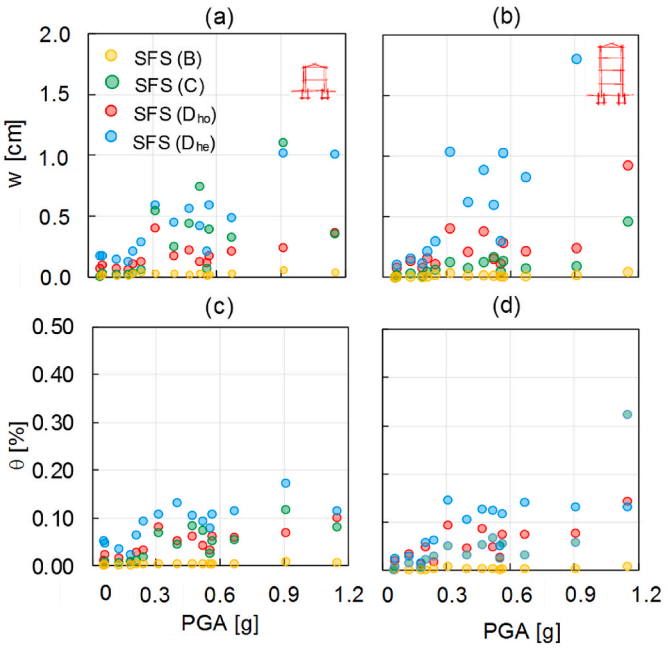

Fig. 17. Scatter plots of the maximum settlement (w), maximum rotation (θ) versus *PGA*, produced by the selected input motions for two-story (a, c) and four-story (b, d) clay brick masonry structures.

The data points in Fig. 18 show the *MIDR*values resulting from NLTHA on fixed-base buildings (black circles) compared with those relevant to compliant-base SFS models, plotted with different colors depending on the soil type. In general, *MIDR*-values of compliant-base models are larger than those predicted on fixed-base models, reflecting the importance of soil amplification and SFSI. Comparing Fig. 18a and b, the variability of the maximum interstory drift appears more affected by the structural slenderness than by the degree of soil deformability, with the highest values pertaining to the tall structures on homogeneous soft soil profile D_{ho}.

The data points are compared to three *MIDR* thresholds associated with the following increasing damage levels (DLs):

- DL1: formation of opening cracks at the toe of a wall, due to the attainment of tensile strength of masonry;
- DL2: activation of the rocking mechanism of masonry walls;
- DL3: near-collapse limit state due to overturning of masonry walls.

The latter damage level was assumed to be the ultimate limit state in which the wall collapse is caused by overturning under out-of-plane motion, which takes place when the interstory drift ratio of the j-th story reaches the following ultimate value [61]:

$$IDR_{u,j} = \frac{t_j}{2h_j} \tag{15}$$

being t_j the masonry wall thickness at the j-th story. In the case of rubble stone masonry, IDR_u is reduced by 35% [62] in order to account for nonlinear effects and possible loss of masonry integrity.

The first damage state (DL1) was assumed to correspond to the formation of opening cracks at the toe of the wall, hence the corresponding threshold is the *IDR* associated with the attainment of the tensile strength in the masonry. The two additional damage states were assumed to be associated with the activation of the rocking mechanism in the structure (DL2) and of the structural collapse due to overturning (DL3). The respective thresholds were defined as the attainment of 25% and 40% of IDR_u.

The comparison between structural demand (*MIDR*) and capacity (*IDR* thresholds associated with each damage level) highlights a higher vulnerability of four-story masonry buildings compared to that of the two-story structures. The motivation behind this outcome is twofold: on one side *MIDR* increases with the building slenderness, and on the other, a lower *IDR* capacity is caused as a result of the reduced masonry thickness of masonry walls at upper stories. Such a difference is enhanced in case of compliant-base models, due to the proximity of the soil and structural fundamental periods, causing double amplification of seismic motion (see comments to Fig. 15). This induces particularly the taller structural models to exceed the *IDR* thresholds associated with the most severe DLs.

5.3. Fragility and damage assessment

After that structural demand and capacity were evaluated, the seismic fragility of the selected SFS models was estimated through the

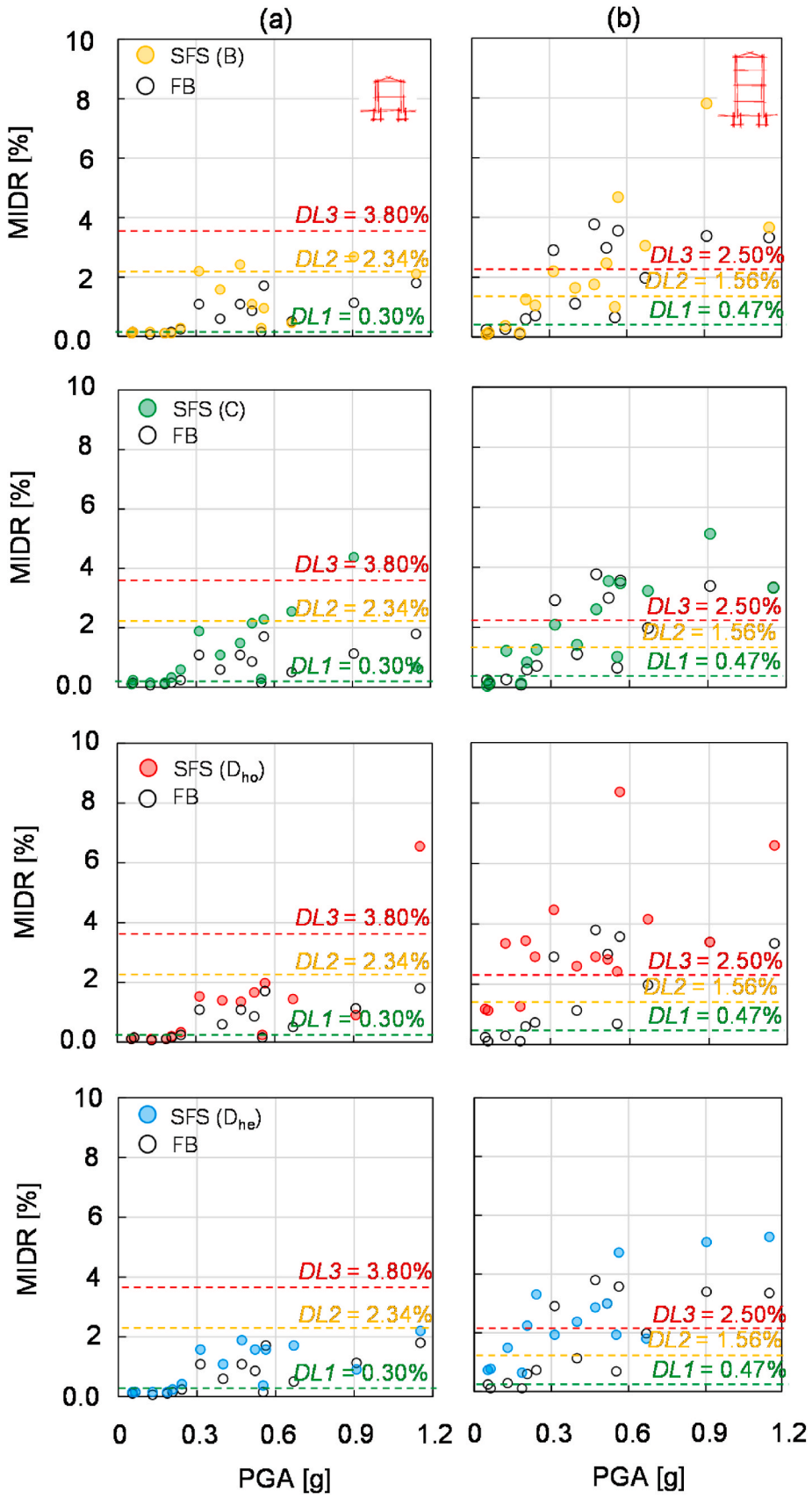

Fig. 18. Scatter plots of *MIDR* versus *PGA* for two-story (a) and four-story (b) clay brick masonry structures.

cloud method [57] as the probability of exceeding a damage level given a seismic intensity measure. Denoting by *IM* the intensity measure assumed to quantify the severity of the reference input motion at the bedrock, seismic fragility was estimated as follows:

$$P[MIDR > MIDR_i|IM] = \Phi\left(\frac{\ln(IM/\eta_{DLi})}{\beta_{DL}}\right) \quad (16)$$

where:

- $MIDR_i$ is the capacity associated with the i-th damage level;
- Φ is the cumulative normal distribution function;
- η_{DLi} and β_{DL} are the median and standard deviation of the lognormal distribution of the *IM* value causing the attainment of $MIDR_i$.

The cloud method assumes a linear relationship between *MIDR* and *IM* in the log-log scale, hence η_{DLi} was estimated as the abscissa of the intersection between the i-th damage threshold and the least squares regression line that fits the (log *IM*, log *MIDR*) data points resulting from NLTHA.

Among several peak, spectral and integral *IM*s that might be related to the seismic damage experienced by a masonry structure, this study considered three ground motion parameters that can reasonably meet the requirements of efficiency, sufficiency and hazard computability [45]: peak ground acceleration (*PGA*), peak ground velocity (*PGV*), and Housner intensity (I_H). This latter *IM* is defined as the integral of spectral velocity $S_v(T)$:

$$I_H = \int_{T_1}^{T_2} S_v(T)dT \quad (17)$$

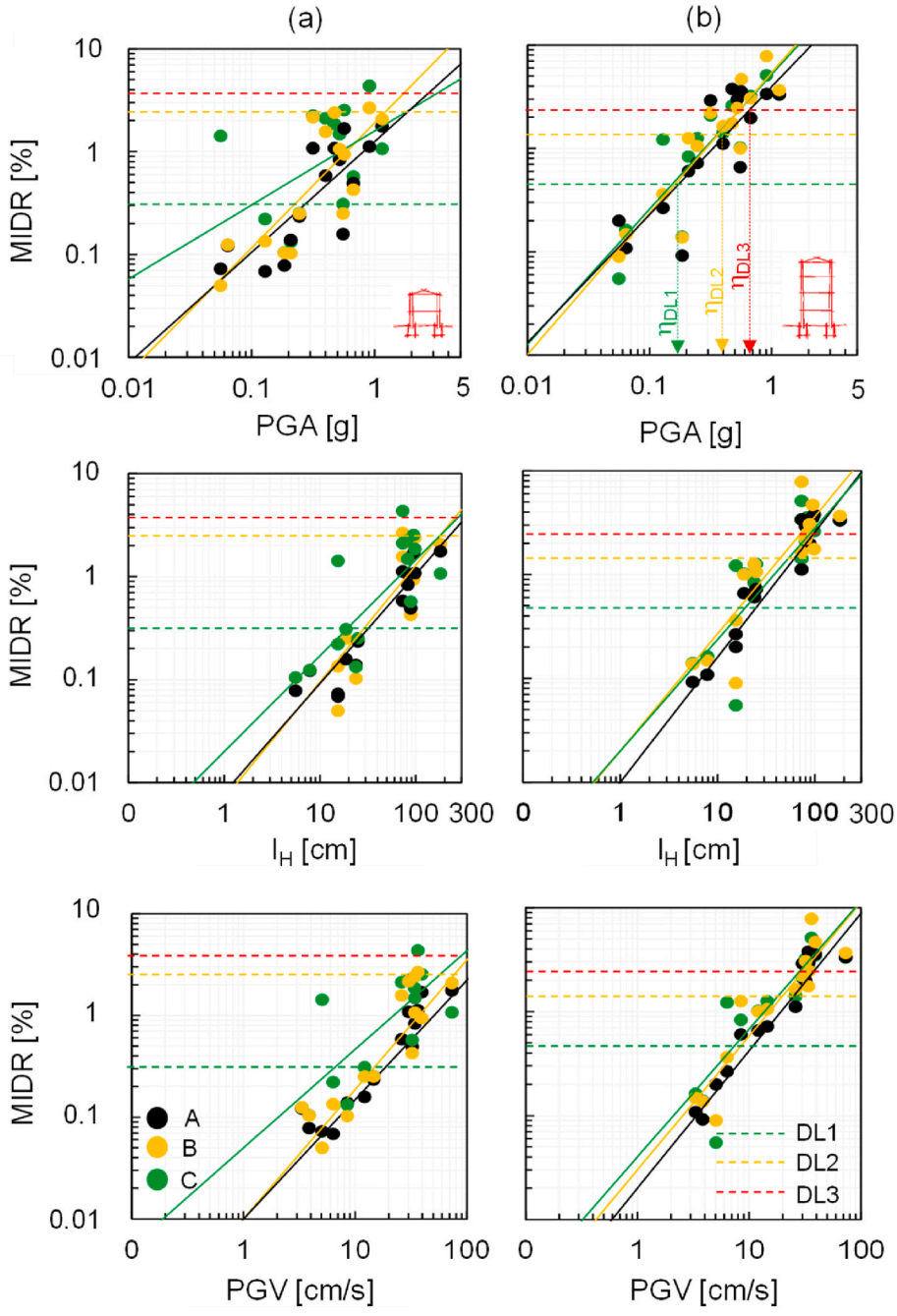

Fig. 19. *EDP–IM* relationships for fixed- and compliant-base models of CBM buildings with (a) $h/b = 1$ and (b) $h/b = 2$.

over the period range [T_1, T_2] equal to [0.1 s, 2.0 s].

As an example, Fig. 19 shows the correlations of the *MIDR* with *PGA*, I_H and *PGV* for clay brick masonry buildings founded on ground types A (black circles), B (yellow circles) and C (green circles). The median values η_{DL1}, η_{DL2} and η_{DL3} are highlighted in Fig. 19b for the four-story structure on type A soil and $IM = PGA$.

The plots in Fig. 19a reveal that the overall trend of *MIDR* vs. each one of the selected *IM*s significantly increases in case of the two-story structures on soil profile C with respect to those founded on ground types A and B. Conversely, the trends appear less dependent on the soil type for the highest aspect ratio h/b (Fig. 19b), implying that the vulnerability of slender masonry buildings, at least on such soil models, is less significantly affected by SFS interaction. It is also worth noting that, for the squat structural model laying on ground type C, the plots of *MIDR* with respect to whatever *IM* are quite scattered and with lower rate of increase (Fig. 19a). This may be due to resonance induced by the proximity of the soil and building fundamental periods, which affects the response under weak to moderate ground motions, but may become less critical when the soil period increases under strong motions.

The efficiency of the selected *IM*s was assessed through the logarithmic standard deviation ($\sigma_{EDP|IM}$) and coefficient of determination (R^2) of the regression model. The best-fit lines computed for all SFS models returned $\sigma_{EDP|IM}$ ranging between 0.27 and 0.79, and R^2 varying between 0.38 and 0.94 [45]. The ranking of *IM*s according to decreasing values of $\sigma_{EDP|IM}$ and increasing values of R^2 revealed that *PGV* and I_H are

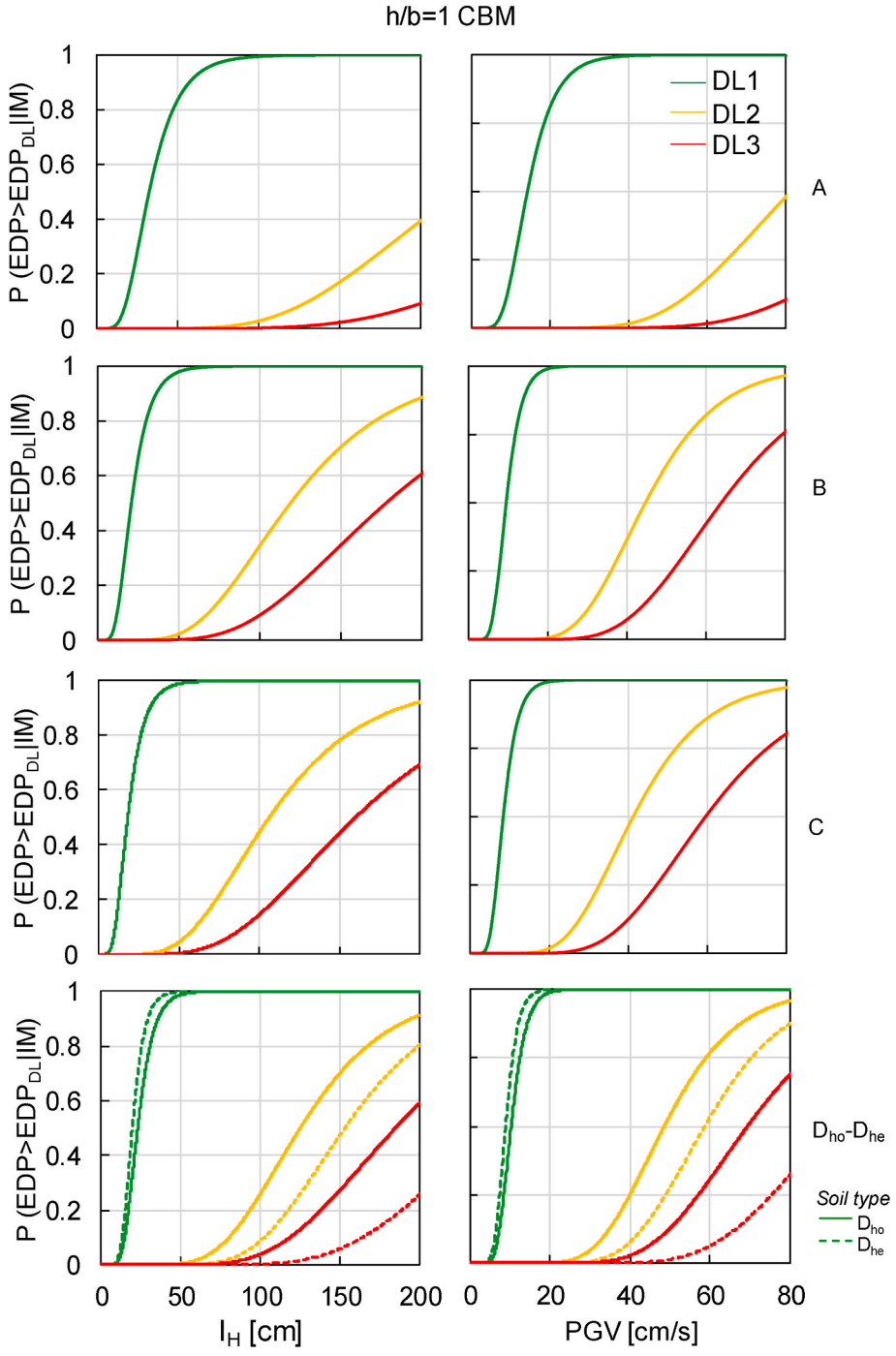

Fig. 20. Fragility curves in terms of I_H and *PGV* of two-story CBM structures ($h/b = 1$) founded on variable soil models.

significantly more efficient than *PGA*. This outcome points out that peak acceleration amplitudes, although often adopted to define seismic vulnerability of low- and medium-rise buildings, are not the best option for predicting structural damage of masonry buildings accounting for SFS interaction.

Accordingly, Fig. 20a and b shows the fragility curves of two-story clay brick masonry buildings with reference to I_H and *PGV*, respectively, for each soil profile under consideration. In all cases, the fragility functions of fixed-base models (ground type A, uppermost plots) are always shifted towards higher *IM* levels compared to compliant-base models on stiff to very soft soils (B, C, D in the lower plots). This implies that neglecting site effects and soil-foundation-structure interaction leads to an underestimation of the probability of damage which overall increases with soil deformability. Rather surprisingly, whatever *IM* is considered, the fragility curves for ground type C plot higher with respect to those relevant to the softer homogeneous soil model, D_{ho}, and these latter in turn predict higher probability of damage than that corresponding to the heterogeneous profile, D_{he}. In this latter case, it was observed that settlements and rotations of the foundation are larger with respect to the homogeneous profile (see Fig. 17), leading to a higher dissipation of seismic energy and a consequent reduction of the *MIDR*.

As a further synthetic summary of the results, each plot in Fig. 21a and b reports the fragility curves relevant to each DL for two-story (dark colour tones) and four-story (light colour tones) clay brick masonry buildings, either in fixed-base conditions or founded on a very soft soil, D_{ho}. It can be observed that the effect of SFSI is significant for both slenderness ratios and apparently increases with the damage level. The increase in seismic fragility due to SFSI can be expressed by the

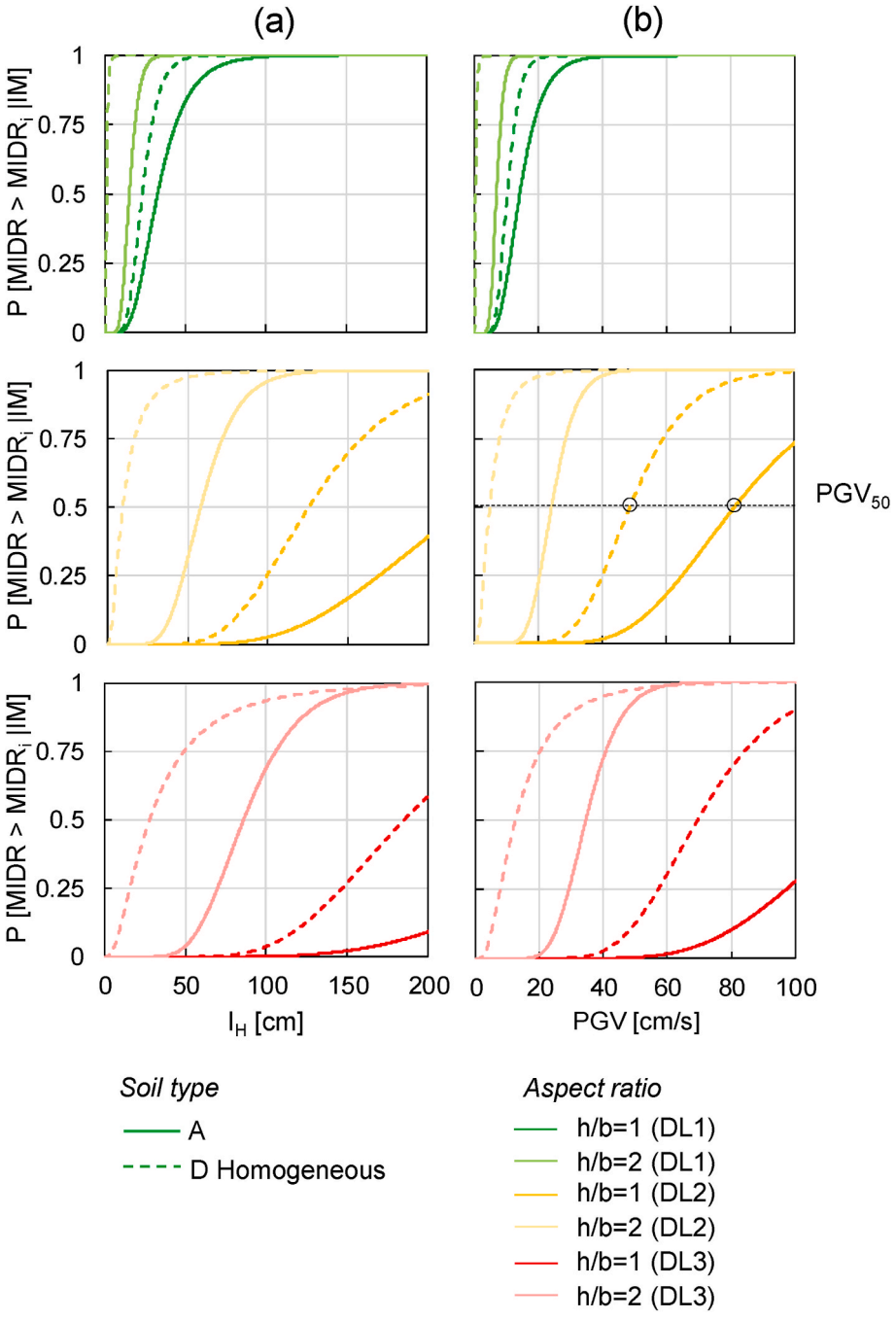

Fig. 21. Fragility curves of two- and four-story CBM structures in terms of (a) I_H and (b) *PGV*.

reduction in median peak ground velocity, PGV_{50}. For example, if the activation of the DL2 of a two-story structure is considered ($h/b = 1$), the median value of *PGV*, shown by the circles in Fig. 21b, is reduced by SFSI from 81 cm/s to 49 cm/s (i.e. by almost 50%).

5.4. Urban-scale application to the village of Onna

The fragility curves developed for SFS models of masonry buildings were implemented at urban scale to be validated against observed damage. Aisa et al. [63] reported a detailed analysis of damage distribution at Onna, a hamlet close to L'Aquila city (Central Italy) in the middle of the Aterno river valley, which was severely struck by a M_W 6.1 earthquake on the April 6, 2009 (Fig. 22a).

The structural typology most widespread in the village corresponds to two- or three-story buildings with rubble stone masonry walls and mixed steel-tile floor systems. Hence, those buildings were assigned a vulnerability class B according to the European Macroseismic Scale EMS-98 [64], which includes (i) masonry structures with irregular texture and efficient connections, and (ii) masonry structures with regular texture and inefficient connections.

Aisa et al. [63] also observed that integrity loss of masonry and OOP mechanisms were the most common failure modes (as exemplified by the picture in Fig. 1b). The above factors motivated the authors of this paper to consider seismic damage to Onna as an interesting case study for validation of the analytical fragility curves presented in Section 5.3.

Fig. 22a shows the shakemap in terms of macroseismic intensity and *PGA* contours of the L'Aquila earthquake mainshock occurred on April 6, 2009, as reported by National Institute of Geophysics and Volcanology. Besides, aerial photos in Fig. 22b show the disruption caused by the earthquake in Onna. In lack of ground motion records in the village area and in order to infer the intensity measures characterizing the site during the mainshock, the bedrock motion at Onna was assimilated to that recorded by the closest seismic station (labelled as AQG). Such an assumption is reasonable, because both AQG station and Onna fall within the surface projection of the fault plane, drawn as a blue rectangle in Fig. 22a. In such conditions and up to a Joyner and Boore source-to-site distance equal to 4 km, ground motion prediction equations are flat (e.g. Bindi et al. [65]): therefore, the recorded signal does not require any scaling.

Since the weathered and fractured rock underlying AQG station is far from being a stiff rock outcrop, the horizontal components of the GM record were first deconvoluted to the bedrock and then projected along the fault parallel (FP) and fault normal (FN) directions [66]. *PGA* was found to be equal to 0.31*g* along both FP and FN directions, while I_H was equal to 91.7 cm and 83.7 cm along them, respectively, due to the impulsive and directivity effects influencing the velocity spectrum.

Fig. 23a shows the distribution of vulnerability classes over the area of Onna, confirming that most of buildings were found pertaining to class B. The *PGA*-values associated with FP and FN directions were used to predict OOP damage to masonry buildings through the fragility curves of the SFS systems. To this aim, the shear wave velocity profiles measured in the alluvial coarse-grained deposit for the seismic microzonation emergency study [67] were firstly examined. Three geophysical surveys were performed, i.e. a MASW test and two refraction microtremors tests (ReMi1 and ReMi2), shown by purple, blue and light blue circles in Fig. 23a. Fig. 23b shows the comparison between the measured shear wave velocity profiles and that adopted in this study for type C soil (see Section 3), which represents the most suitable soil category for the site of Onna.

Fig. 24a shows the territorial distribution of the observed damage as classified by [64] for vulnerability class B according to the EMS-98 scale, which identifies the following six damage levels:

- D0: no damage;
- D1: development of few cracks in several walls;
- D2: significant cracks in many walls and collapse of plaster;
- D3: development of extensive and wide cracks in many walls;
- D4: significative damage to walls or partial structural collapse of roofs;
- D5: destruction of the structure.

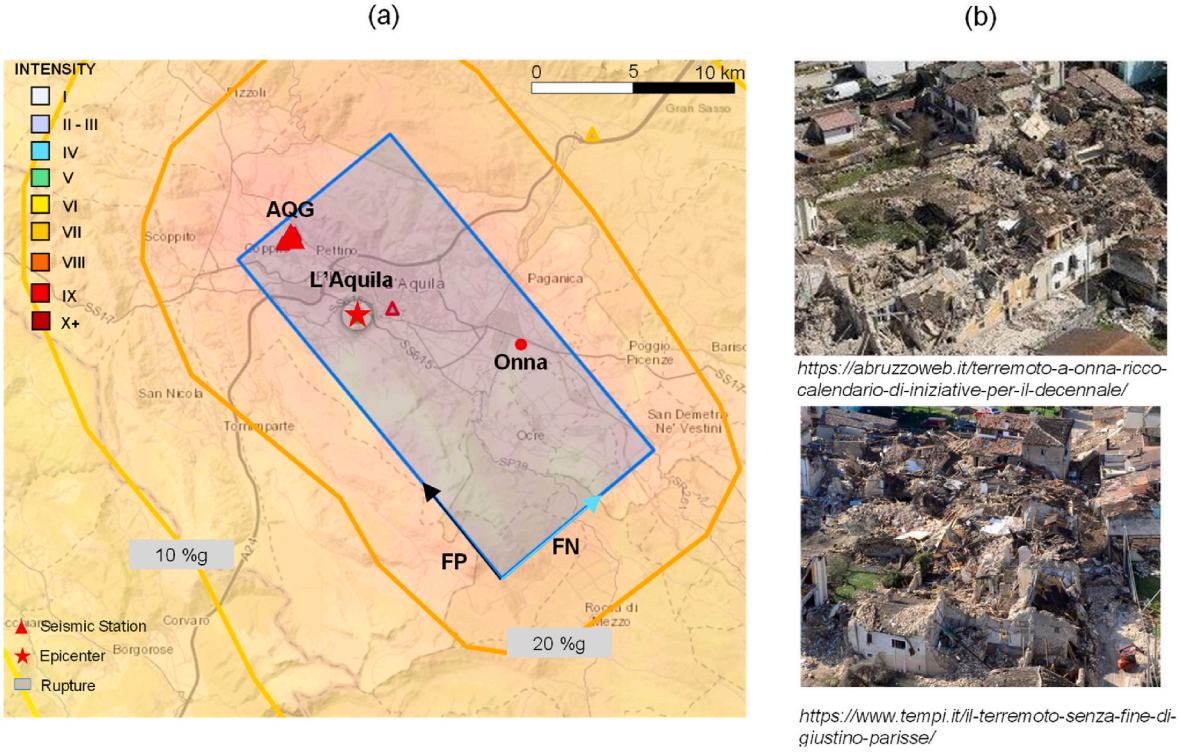

Fig. 22. (a) Shakemap in terms of macroseismic intensity and *PGA* of the M_W 6.1 seismic event on April 6, 2009 (http://shakemap.ingv.it/shake4/viewLeaflet.html?eventid=1895389); (b) aerial views of damage to masonry buildings located in the Onna village.

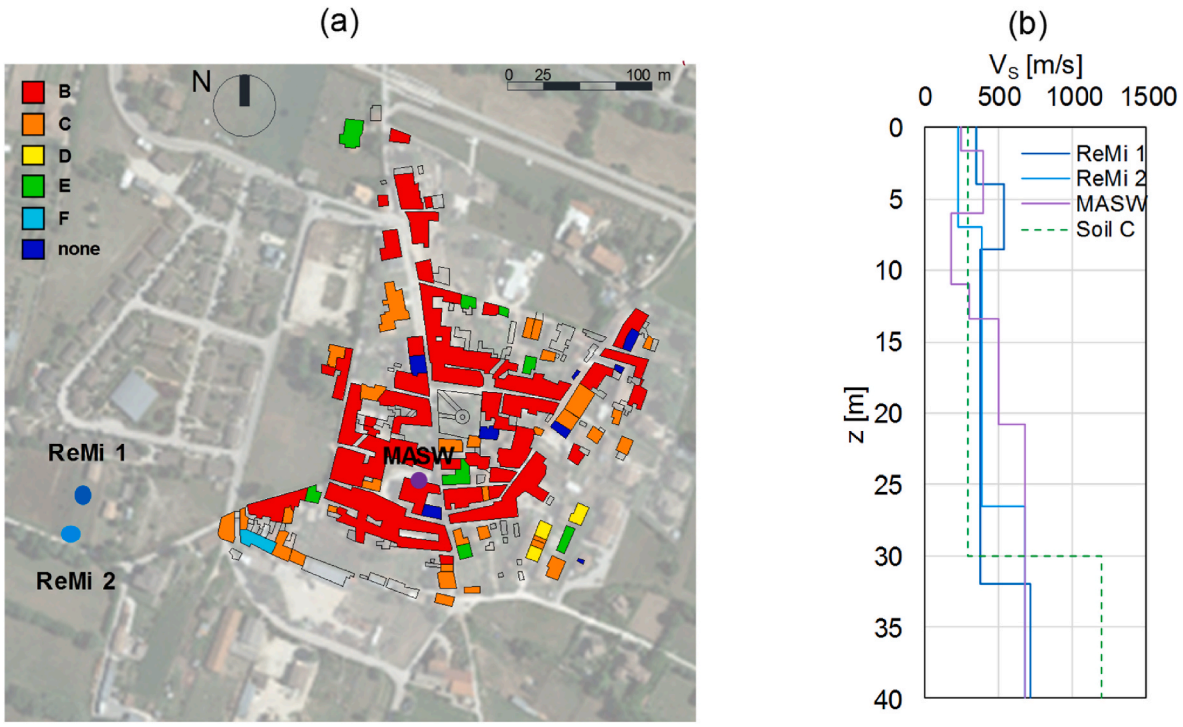

Fig. 23. (a) Distribution of vulnerability classes according to EMS-98 [64] with location of geophysical surveys (ReMi 1, ReMi 2 and MASW); (b) shear wave velocity profiles.

In order to compare such damage levels with the thresholds defined in the fragility study (see Section 5.3), D1 was not considered consistently with the 2D models assumed in this study, D2 was associated with DL1, D3 and D4 were merged with each other and assimilated to DL2, and D5 was associated with DL3.

Fig. 24b shows the comparison between the fragility curves computed in this study for the same kind of masonry buildings (rubble stone, $h/b = 1$) founded on homogeneous type C soil, in terms of *PGA* (as the most commonly used *IM*) and of the optimal *IM*s for this soil-structure combination, i.e. *PGV* and Housner Intensity computed between 0.1 s and 2.0 s. The vertical arrows in Fig. 24b show the percentage of each damage level relevant to the values of *PGA*, *PGV* and I_H associated with the FN and FP components of the reference bedrock motion inferred at Onna.

The histograms in Fig. 24c show the comparison between the observed and predicted damage distributions, the latter derived by computing the difference between the probabilities of exceeding DL_i and DL_{i+1}. It can be observed that the use of *PGA* as *IM* can lead to significant overestimation of damage at DL2, the opposite occurring for DL3 or higher damage levels. Instead, an increasingly better agreement with the observed distribution was found at all damage levels using *PGV* and spectral intensity I_H as intensity measures.

6. Conclusions and perspectives

This paper has presented the main methodological outcomes of a long-term comprehensive study, which was developed by the authors with the purpose of calibrating up-to-date straightforward tools to account for soil-foundation-structure interaction in the assessment of the seismic safety of URM buildings against out-of-plane mechanisms.

A parametric study was carried out to assess the role of several factors on the dynamic response and seismic fragility of 2D models representative of URM building sections with load-bearing walls resting on shallow foundations embedded in a subsoil subjected to horizontal ground motions.

The influence of the following factors was investigated:

(i) the masonry type, i.e. tuff stone masonry, rubble stone masonry or clay brick masonry;
(ii) the building slenderness, namely, the height-to-width (aspect) ratio of the above-ground building structure;
(iii) the soil-structure stiffness ratio;
(iv) the degree of inhomogeneity in the subsoil profile.

To analyze the effects of the soil properties, the Eurocode-conforming ground types A, B, C and D were considered, leading to the analysis of four homogeneous subsoil models, one heterogeneous very soft soil profile and three-layered subsoil models (D-B, D-C and C–B) consisting of a loose cover overlying a stiffer in-depth formation.

A first part of the study was addressed to the linear dynamic analysis of tuff stone masonry building configurations settled on the above-mentioned subsoil models, using both coupled continuum SFS models and single-degree-of-freedom systems with rigid or compliant base (i.e. the so-called 'replacement oscillator'). Based on an equivalent soil-structure stiffness ratio the comparison between analysis results of continuum models and the dynamic response of the 'replacement oscillator' permitted to develop a simplified procedure that can be used to estimate the elongation of the fundamental period and the increase in radiation damping due to the SFS interaction.

The above procedure was developed to be applicable to SFS systems for which some critical factors may be overlooked by assuming simplified hypotheses, such as URM buildings with irregular geometry (above and/or below ground) and shallow flexible foundations in layered soil. The method was proved to be effectively applied at urban scale for the city of Matera, allowing a significant validation against on-site measurements of soil-building fundamental frequency. Once soil nonlinearity and overall system damping are appropriately considered, the method can be fruitfully adopted for the assessment of the seismic demand on structures and foundations, using free-field response spectra derived from seismic response analyses, at both local and territorial scales.

In the second part of the study, the seismic damage and fragility of SFS systems representative of 2D building sections laying on different

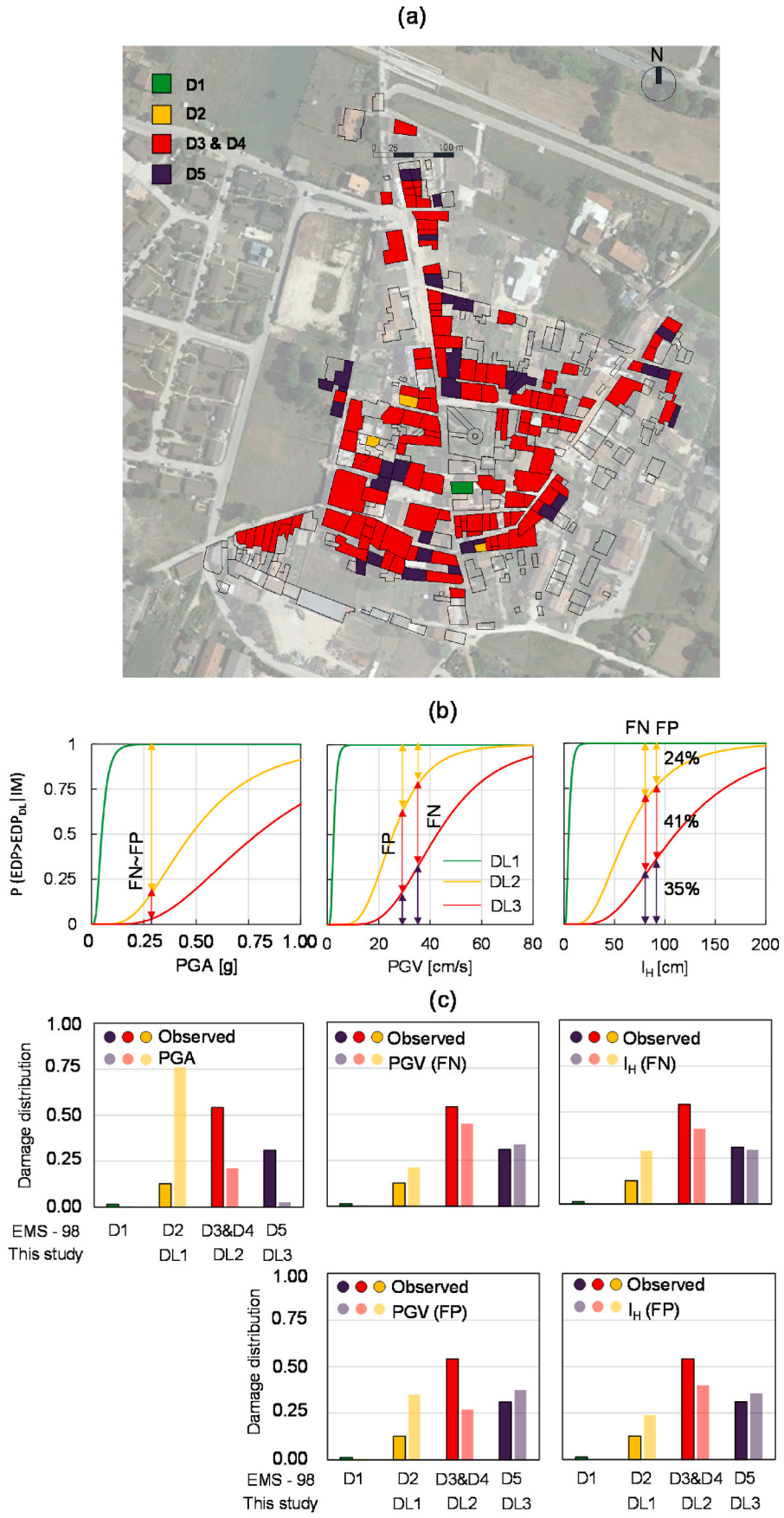

Fig. 24. (a) Territorial damage distribution at Onna for vulnerability class B; (b) SFS fragility functions for rubble stone masonry buildings with $h/b = 1$ founded on ground type C; (c) comparison between statistical distributions of observed and predicted damage.

subsoil models subjected to out-of-plane excitation was investigated. A set of natural accelerograms associated with wide ranges of PGA, moment magnitude and epicentral distance, was selected by following the so-called 'cloud method' and used a reference input motions in time history analyses where the behavior of both soil and masonry was assumed as nonlinear.

In case of two-story buildings, analysis results highlighted an amplification or de-amplification of seismic demand in terms of PGA and spectral acceleration at the foundation level with respect to bedrock, depending on whether a weak or a strong ground motion was considered. In this respect, the ground motion amplification increased particularly in the case of heterogeneous soil model. By contrast, four-story building models were found to experience a significant amplification regardless of the ground motion intensity, also exhibiting double-resonance effects due to both input motion–soil and soil–structure couplings.

The maximum settlement and tilting rotation of the foundation system were also investigated, highlighting more significant site amplification and SFS effects in the case of four-story buildings, due to their more pronounced rocking motion. In such conditions, assuming homogeneous stiffness and strength profiles for a soft soil deposit pertaining to ground type D may produce unconservative predictions in terms of settlements and tilting rotations, hence underestimating the seismic demand on foundations. The opposite effect was observed in case of two-story buildings on stiffer type C soil, as a result of the variability in soil-building resonance conditions.

The fragility of the selected SFS systems was expressed using several intensity measures and maximum interstory drift ratio, *MIDR*, as an engineering demand parameter. Analysis results showed that the variability of *MIDR* is more significantly influenced by the building aspect ratio than soil deformability, showing the highest levels of seismic demand in the case of four-story buildings on homogeneous soft soil. Overall, fragility curves corresponding to increasing level of out-of-plane damage of URM walls were found to be highly dependent on the building aspect ratio. In the case of two-story buildings, seismic fragility is apparently sensitive to the soil type, while SFS interaction produces lower impact in case of slender buildings.

Among the different intensity measures suitable to describe the fragility of such SFS systems, *PGV* and I_H were found to be significantly more efficient than *PGA*, remarking that peak ground acceleration may not be the best option to predict damage to masonry buildings when SFS interaction is taken into account. In all cases, neglecting site effects and SFS interaction led to underestimate seismic fragility, which overall increases with soil deformability.

The proposed fragility curves for typical SFS systems of URM buildings as a function of ground motion intensity at bedrock can support damage assessments at a territorial scale, e.g. by a 'convolution' of shakemaps through site and building classification datasets. In this context, the consistency between the statistical distributions of damage predicted and observed in the village of Onna, central Italy, after the 2009 L'Aquila earthquake provides an encouraging example of application.

The outcomes of this study highlight several trajectories for potential developments in the near future addressed to reduce the limitations and to improve the reliability of the methods proposed. First of all, the numerical investigation should be extended to a wider set of building geometries and materials, subsoil properties and damage mechanisms. The use of both 2D and 3D coupled models may enable to assess the seismic performance and fragility of URM buildings prone to suffer more complex damage mechanisms, such as corner failure, horizontal bending failure of spandrels, and two-way bending failure of walls. This applies not only to the procedure for predicting the elongation of fundamental period and the variation of equivalent damping, but also to the assessment of fragility accounting for nonlinear SFS interaction. The proposed fragility analysis, which directly refers to intensity measures of the reference input motion, should be further compared against alternative approaches where, for instance, the probability of damage is referred to the ground motion intensity including site amplification. Finally, validation of these procedures and fragility models should be strengthened against additional case studies, where accurate inventories of observed damage are available together with seismic motions recorded on both ground surface and building structure.

Author statement

FRANCESCO SILVESTRI: Conceptualization, Methodology, Writing - Review & Editing, Visualization, Funding acquisition, Project administration, Supervision. FILOMENA DE SILVA: Conceptualization, Methodology, Writing - Original Draft, Writing - Review & Editing, Visualization. ANNACHIARA PIRO: Conceptualization, Methodology, Formal analysis, Data curation, Writing - Original Draft, Writing - Review & Editing, Visualization. FULVIO PARISI: Conceptualization, Methodology, Writing - Review & Editing, Visualization, Project administration.

Declaration of competing interest

The authors declare that they have no known competing financial interests or personal relationships that could have appeared to influence the work reported in this paper.

Data availability

Data will be made available on request.

Acknowledgements

This work was carried out as part of WP16.3 "Soil-Foundation-Structure Interaction" and WP4.9 "Multi-Risk Assessment and Mitigation Strategies" in the framework of the research programme funded by Italian Civil Protection through the ReLUIS Consortium (DPC-ReLUIS 2022–2024).

References

[1] Independent Evaluation Group (IEG). Development actions and the rising incidence of disasters. Washington, DC: The World Bank; 2007.
[2] Giardini D, Al E. Seismic hazard harmonization in Europe (SHARE): online data resource. 2013. https://doi.org/10.12686/SED-00000001-SHARE. 2013.
[3] Crowley H, Silva V, Crowley H, Rodrigues D. The European seismic risk model 2020 (ESRM 2020) the European seismic risk model 2020 (ESRM 2020). ICONHIC2019 2nd. Int Conf Nat Hazards Infrastruct 2019:2020.
[4] Augenti N, Parisi F. Learning from construction failures due to the 2009 L'aquila, Italy, earthquake. J Perform Constr Facil 2010;24:536–55. https://doi.org/10.1061/(asce)cf.1943-5509.0000122.
[5] Dolce M, Di Bucci D. Comparing recent Italian earthquakes. Bull Earthq Eng 2017; 15:497–533. https://doi.org/10.1007/s10518-015-9773-7.
[6] Parisi F, Augenti N. Earthquake damages to cultural heritage constructions and simplified assessment of artworks. Eng Fail Anal 2013;34:735–60. https://doi.org/10.1016/j.engfailanal.2013.01.005.
[7] Vlachakis G, Vlachaki E, Lourenço PB. Learning from failure: damage and failure of masonry structures, after the 2017 Lesvos earthquake (Greece). Eng Fail Anal 2020;117. https://doi.org/10.1016/j.engfailanal.2020.104803.
[8] Yakut A, Sucuoğlu H, Binici B, Canbay E, Donmez C, İlki A, et al. Performance of structures in İzmir after the Samos island earthquake. Bull Earthq Eng 2021. https://doi.org/10.1007/s10518-021-01226-6.
[9] Atalić J, Uroš M, Šavor Novak M, Demšić M, Nastev M. The Mw5.4 Zagreb (Croatia) earthquake of March 22, 2020: impacts and response. Bull Earthq Eng 2021;19. https://doi.org/10.1007/s10518-021-01117-w.
[10] Daniell JE, Khazai B, Wenzel F, Vervaeck A. The CATDAT damaging earthquakes database. Nat Hazards Earth Syst Sci 2011. https://doi.org/10.5194/nhess-11-2235-2011.
[11] Kausel E. Early history of soil-structure interaction. Soil Dynam Earthq Eng 2010; 30:822–32. https://doi.org/10.1016/j.soildyn.2009.11.001.
[12] Mylonakis G, Gazetas G. Seismic soil-structure interaction: beneficial or detrimental? J Earthq Eng 2000;4:277–301. https://doi.org/10.1080/13632460009350372.
[13] Khosravikia F, Mahsuli M, Ghannad MA. The effect of soil–structure interaction on the seismic risk to buildings. Bull Earthq Eng 2018;16:3653–73. https://doi.org/10.1007/s10518-018-0314-z.

[14] Karapetrou ST, Fotopoulou SD, Pitilakis KD. Seismic vulnerability assessment of high-rise non-ductile RC buildings considering soil-structure interaction effects. Soil Dynam Earthq Eng 2015;73:42–57. https://doi.org/10.1016/j.soildyn.2015.02.016.

[15] Mitropoulou CC, Kostopanagiotis C, Kopanos M, Ioakim D, Lagaros ND. Influence of soil-structure interaction on fragility assessment of building structures. Structures 2016;6. https://doi.org/10.1016/j.istruc.2016.02.005.

[16] Mashhadi S, Asadi A, Homaei F, Tajammolian H. Seismic response of mid-rise steel MRFs: the role of geometrical irregularity, frequency components of near-fault records, and soil-structure interaction. Bull Earthq Eng 2021;19. https://doi.org/10.1007/s10518-021-01103-2.

[17] Hamidia M, Shokrollahi N, Nasrolahi M. Soil-structure interaction effects on the seismic collapse capacity of steel moment-resisting frame buildings. Structures 2021;32. https://doi.org/10.1016/j.istruc.2021.03.068.

[18] de Silva F, Ceroni F, Sica S, Silvestri F. Non-linear analysis of the Carmine bell tower under seismic actions accounting for soil–foundation–structure interaction. Bull Earthq Eng 2018;16:2775–808. https://doi.org/10.1007/s10518-017-0298-0.

[19] Brunelli A, de Silva F, Cattari S. Site effects and soil-foundation-structure interaction: derivation of fragility curves and comparison with Codes-conforming approaches for a masonry school. Soil Dynam Earthq Eng 2020;154:107125. https://doi.org/10.1016/j.soildyn.2021.107125.

[20] Petridis C, Pitilakis D. Fragility curve modifiers for reinforced concrete dual buildings, including nonlinear site effects and soil–structure interaction. Earthq Spectra 2020. https://doi.org/10.1177/8755293020919430.

[21] D'Ayala D, Speranza E. Definition of collapse mechanisms and seismic vulnerability of historic masonry buildings. Earthq Spectra 2003;19:479–509. https://doi.org/10.1193/1.1599896.

[22] Fathi A, Sadeghi A, Emami Azadi MR, Hoveidae N. Assessing the soil-structure interaction effects by direct method on the out-of-plane behavior of masonry structures (case study: arge-Tabriz). Bull Earthq Eng 2020;18:6429–43. https://doi.org/10.1007/s10518-020-00933-w.

[23] Gazetas G. Formulas and charts for impedances of surface and embedded foundations. J Geotech Eng 1991. https://doi.org/10.1061/(ASCE)0733-9410(1991)117:9(1363).

[24] Amendola C, de Silva F, Vratsikidis A, Pitilakis D, Anastasiadis A, Silvestri F. Foundation impedance functions from full-scale soil-structure interaction tests. Soil Dynam Earthq Eng 2021;141:106523. https://doi.org/10.1016/j.soildyn.2020.106523.

[25] Tileylioglu S, Stewart JP, Nigbor RL. Dynamic stiffness and damping of a shallow foundation from forced vibration of a field test structure. J Geotech Geoenviron Eng 2011;137:344–53. https://doi.org/10.1061/(asce)gt.1943-5606.0000430.

[26] Pais A, Kausel E. Approximate formulas for dynamic stiffnesses of rigid foundations. Soil Dynam Earthq Eng 1988;7. https://doi.org/10.1016/S0267-7261(88)80005-8.

[27] Liou GS. Impedance for rigid square foundation on layered medium. Doboku Gakkai Rombun-Hokokushu/Proceedings Japan Soc Civ Eng; 1993. https://doi.org/10.2208/jscej.1993.471_47.

[28] Pitilakis D, Moderessi-Farahmand-Razavi A, Clouteau D. Equivalent-linear dynamic impedance functions of surface foundations. J Geotech Geoenviron Eng 2013;139:1130–9. https://doi.org/10.1061/(asce)gt.1943-5606.0000829.

[29] de Silva F, Amendola C, Pitilakis D, Silvestri F. Prediction of foundation stiffness and damping ratio under horizontal translation and rocking motion. Soil Dynam Earthq Eng 2023;166:107735. https://doi.org/10.1016/J.SOILDYN.2022.107735.

[30] Cremer C, Pecker A, Davenne L. Cyclic macro-element for soil-structure interaction: material and geometrical non-linearities. Int J Numer Anal Methods GeoMech 2001;25. https://doi.org/10.1002/nag.175.

[31] Cremer C, Pecker A, Davenne L. Modelling of nonlinear dynamic behaviour of a shallow strip foundation with macro-element. J Earthq Eng 2002;6. https://doi.org/10.1080/13632460209350414.

[32] Veletsos AS, Meek JW. Dynamic behaviour of building-foundation systems. Earthq Eng Struct Dynam 1974;3:121–38. https://doi.org/10.1002/eqe.4290030203.

[33] Maravas A, Mylonakis G, Karabalis DL. Simplified discrete systems for dynamic analysis of structures on footings and piles. Soil Dynam Earthq Eng 2014. https://doi.org/10.1016/j.soildyn.2014.01.016.

[34] Piro A, de Silva F, Parisi F, Scotto di Santolo A, Silvestri F. Effects of soil-foundation-structure interaction on fundamental frequency and radiation damping ratio of historical masonry building sub-structures. Bull Earthq Eng 2020;18:1187–212. https://doi.org/10.1007/s10518-019-00748-4.

[35] Gaudio D, Rampello S. On the assessment of seismic performance of bridge piers on caisson foundations subjected to strong ground motions. Earthq Eng Struct Dynam 2021;50:1429–50. https://doi.org/10.1002/eqe.3407.

[36] Augenti N, Parisi F. Teoria e tecnica delle strutture in muratura. Milan, Italy: Hoepli; 2019 (In Italian).

[37] Winterkorn Hans F, Fang H-Y. Foundation engineering handbook. Newyork,US: Van Nostrand Reinhold; 1991.

[38] Tropeano G, Soccodato FM, Silvestri F. Re-evaluation of code-specified stratigraphic amplification factors based on Italian experimental records and numerical seismic response analyses. Soil Dynam Earthq Eng 2018;110. https://doi.org/10.1016/j.soildyn.2017.12.030.

[39] CEN. Eurocode 8: design of structures for earthquake resistance – Part 1: general rules, seismic actions and rules for buildings. 2004.

[40] Capatti MC, Tropeano G, Morici M, Carbonari S, Dezi F, Leoni G, et al. Implications of non-synchronous excitation induced by nonlinear site amplification and of soil-structure interaction on the seismic response of multi-span bridges founded on piles. Bull Earthq Eng 2017;15:4963–95. https://doi.org/10.1007/s10518-017-0165-z.

[41] Augenti N, Parisi F. Constitutive models for tuff masonry under uniaxial compression. J Mater Civ Eng 2010;22:1102–11. https://doi.org/10.1061/(ASCE)MT.1943-5533.0000119.

[42] Stokoe KH, Darendeli MB, Menq F, Choi WK. Comparison of the linear and nonlinear dynamic properties of gravels , sands , silts and clays. Proc. 11th Int. Conf. Soil Dyn. Earthq. Eng. 2004.

[43] Seed HB, Idriss IM. Soil moduli and damping factors for dynamic response analysis. Rep No UCB/EERC-70/L0. Berkeley, December: Univ California; 1970.

[44] Vucetic M, Dobry R. Effect of soil plasticity on cyclic response. J Geotech Eng 1991;117:89–107. https://doi.org/10.1061/(ASCE)0733-9410(1991)117:1(89).

[45] Piro A. Soil - structure interaction effects on seismic response of masonry buildings. University of Naples Federico II; 2021.

[46] MIT Ministero delle infrastrutture e dei trasporti. Circolare 21 gennaio 2019, n. 7 Istruzioni per l'applicazione dell'«Aggiornamento delle "Norme tecniche per le costruzioni"». Gazz Uff Della Repubb Ital; 2019 (In Italian).

[47] Itasca. FLAC version 7.0 fast Lagrangian analysis of continua. 2011.

[48] Kuhlemeyer RL, Lysmer J. Finite element method accuracy for wave propagation problems. J Soil Mech Found Div 1973;99:421–7. https://doi.org/10.1061/JSFEAQ.0001885.

[49] Stewart JP, Kim S, Bielak J, Dobry R, Power MS. Revisions to soil-structure interaction procedures in NEHRP design provisions. Earthq Spectra 2003;19:677–96. https://doi.org/10.1193/1.1596213.

[50] Dobry R, Oweis I, Urzua A. Simplified procedures for estimating the fundamental period of a soil profile. Bull Seismol Soc Am 1976;66:1293–321.

[51] de Silva F, Pitilakis D, Ceroni F, Sica S, Silvestri F. Experimental and numerical dynamic identification of a historic masonry bell tower accounting for different types of interaction. Soil Dynam Earthq Eng 2018;109:235–50. https://doi.org/10.1016/j.soildyn.2018.03.012.

[52] Gazetas G. Foundation vibrations. Found. Eng. Handb. Boston, MA: Springer US; 1991. p. 553–93. https://doi.org/10.1007/978-1-4615-3928-5_15.

[53] Tragni N, Calamita G, Lastilla L, Belloni V, Ravanelli R, Lupo M, et al. Sharing soil and building geophysical data for seismic characterization of cities using Clara Webgis: a case study of matera (southern Italy). Appl Sci 2021;11. https://doi.org/10.3390/app11094254.

[54] Gallipoli MR, Calamita G, Tragni N, Pisapia D, Lupo M, Mucciarelli M, et al. Evaluation of soil-building resonance effect in the urban area of the city of Matera (Italy). Eng Geol 2020;272:105645. https://doi.org/10.1016/j.enggeo.2020.105645.

[55] Piro A, Tragni N, de Silva F, Parisi F, Gallipoli MR, Silvestri F. Validation of a simplified approach for evaluating soil-structure interaction effects on the seismic response of masonry buildings. In: Third eur. Conf. Earthq. Eng. Seismol. 4-9 sept. 2022. Bucharest, Rom.: Int. Conf. Centre; 2022.

[56] Piro A, Tragni N, de Silva F, Calamita G, Cristallo FM, Gallipoli MR, et al. Uno studio sperimentale e analitico sugli effetti dell'interazione terreno-struttura in un quartiere di Matera. Atti dell'Incontro Annu. dei Ric. di Geotec. – IARG 2022. Roma: Edizioni AGI; 2022. ISBN 9788897517108 (In Italian).

[57] Jalayer F, De Risi R, Manfredi G. Bayesian Cloud Analysis: efficient structural fragility assessment using linear regression. Bull Earthq Eng 2015;13:1183–203. https://doi.org/10.1007/s10518-014-9692-z.

[58] Smerzini C, Galasso C, Iervolino I, Paolucci R. Ground motion record selection based on broadband spectral compatibility. Earthq Spectra 2014;30:1427–48. https://doi.org/10.1193/052312EQS197M.

[59] Holtz RD. Stress distribution and settlement of shallow foundations. Found. Eng. Handb.; 1991. p. 166–222. https://doi.org/10.1007/978-1-4757-5271-7_5.

[60] Polshin DE, Tokar RA. Maximum allowable non-uniform settlement of structures. 4th Int Conf Soil Mech Found Eng 1957;1:402–5.

[61] Lagomarsino S. Seismic assessment of rocking masonry structures. Bull Earthq Eng 2015;13:97–128. https://doi.org/10.1007/s10518-014-9609-x.

[62] De Felice G. Out-of-plane seismic capacity of masonry depending on wall section morphology. Int J Architect Herit 2011;5:466–82. https://doi.org/10.1080/15583058.2010.530339.

[63] Aisa E, De Maria A, De Sortis A, Nasini U. Analisi del danneggiamento di Onna (L'Aquila) durante il sisma del 6 Aprile 2009. Ing Sismica 2011;28:63–74.

[64] Grünthal G. European macroseismic scale 1998 (EMS-98). Cahiers du Centre Européen de Géodynamique et de Séismologie 15, vol. 15; 1998.

[65] Bindi D, Pacor F, Luzi L, Puglia R, Massa M, Ameri G, et al. Ground motion prediction equations derived from the Italian strong motion database. Bull Earthq Eng 2011;9. https://doi.org/10.1007/s10518-011-9313-z.

[66] Evangelista L, Landolfi L, d'Onofrio A, Silvestri F. The influence of the 3D morphology and cavity network on the seismic response of Castelnuovo hill to the 2009 Abruzzo earthquake. Bull Earthq Eng 2016. https://doi.org/10.1007/s10518-016-0011-8.

[67] Gruppo di Lavoro MS–AQ. Microzonazione sismica per la ricostruzione dell'area aqui-lana. Regione Abruzzo – dipartimento della Protezione Civile. 3 vol. e Cd-rom.5 L'Aquila 2010;II:199–221 (in Italian).